

Auto-differentiable data assimilation: Co-learning of states, dynamics, and filtering algorithms

Melissa Adrian^{*1}, Daniel Sanz-Alonso², and Rebecca Willett^{2,3,4}

¹School of Mechanical Engineering, Purdue University, West Lafayette, IN 47907

²Department of Statistics, The University of Chicago, Chicago, IL 60637

³Department of Computer Science, The University of Chicago, Chicago, IL 60637

⁴NSF-Simons National Institute for Theory and Mathematics in Biology, Chicago, IL 60611

March 24, 2026

Abstract

Data assimilation algorithms estimate the state of a dynamical system from partial observations, where the successful performance of these algorithms hinges on costly parameter tuning and on employing an accurate model for the dynamics. This paper introduces a framework for jointly learning the state, dynamics, and parameters of filtering algorithms in data assimilation through a process we refer to as auto-differentiable filtering. The framework leverages a theoretically motivated loss function that enables learning from partial, noisy observations via gradient-based optimization using auto-differentiation. We further demonstrate how several well-known data assimilation methods can be learned or tuned within this framework. To underscore the versatility of auto-differentiable filtering, we perform experiments on dynamical systems spanning multiple scientific domains, such as the Clohessy-Wiltshire equations from aerospace engineering, the Lorenz-96 system from atmospheric science, and the generalized Lotka-Volterra equations from systems biology. Finally, we provide guidelines for practitioners to customize our framework according to their observation model, accuracy requirements, and computational budget.

1 Introduction

In many applied scientific settings, practitioners have access to observational data that provides a partial and noisy snapshot of a dynamical system. This data may be utilized for a variety of purposes, including inferring interpretable parameters of the system, improving forecast skill, and reconstructing the underlying state of the system in the past. However, the noisy and incomplete nature of these observations poses significant challenges for both inference and prediction. *Data assimilation* provides a class of methods to combine data sources of various modalities, denoise, and “fill in the gaps” in a principled way.

Data assimilation was proposed in Richardson (1922) for atmospheric state estimation with the goal of improving weather prediction. Early data assimilation methods include the Kalman filter (Kalman, 1960) and optimal interpolation (Gandin, 1966), which handle assimilating observations from linear systems, both in terms of dynamics and observation models. As the need increased for data assimilation algorithms that could handle nonlinearities, the variational approaches 3DVar (Lorenc, 1986) and 4DVar (Courtier et al., 1994) were developed. The landscape for data assimilation significantly changed when ensemble-based methods (Palmer et al., 1992) were introduced, allowing for improved notions of uncertainty quantification for nonlinear systems. A prototypical ensemble-based data assimilation method is the ensemble Kalman filter (Evensen, 1994, 2003, EnKF), which inspired hybrid variational-ensemble approaches such as the ensemble 3DVar (Hamill and Snyder, 2000, Ens3DVar) and the ensemble 4DVar (Liu et al., 2008, Ens4DVar). Among these choices, there is no one catch-all algorithm; practitioners weigh each approach’s advantages and disadvantages and choose the algorithm that balances specific considerations for their applied needs.

One important challenge in data assimilation is that the dynamics model governing the evolution of the state is often expensive to simulate and subject to model error. A recent and promising approach to alleviate these issues is to leverage machine-learned surrogate models for the dynamics (Chen, 2023; Bach et al., 2025b; Adrian et al., 2025; Sanz-Alonso and Waniorek, 2025; Chakraborty et al., 2025). The wide success of machine learning in building surrogates, particularly in emulating physical systems, can be attributed to the open availability of high-quality training data. In many domains, expensive processing to curate this high-quality training data

*Corresponding author: madrian@purdue.edu

needs to occur before surrogate learning even begins. Particularly for high-dimensional settings, fine-grained information may not be readily available, and data assimilation algorithms may be required to distill fine-scale features from coarse measurements. Thus, there is a bidirectional relationship between machine learning and data assimilation: data assimilation algorithms benefit from machine-learned dynamics models, and machine learning surrogate models benefit from training data processed using data assimilation algorithms.

Data assimilation algorithms, though essential in many applications, require substantial tuning before they can be deployed in practice. For example, in 3DVar a background covariance matrix describing the time-independent covariances of forecast errors needs to be curated prior to using this algorithm. In atmospheric data assimilation, the background error covariance has been traditionally estimated via the National Meteorological Center (NMC) method (Parrish and Derber, 1992), which aims to estimate this error covariance matrix in the absence of complete ground truth data. Moreover, parameters such as covariance inflation and the covariance mixing parameter in ensemble schemes additionally require prior specification, requiring multiple runs of the algorithm for tuning.

In this paper, we present a general framework that allows for learning updates to the dynamics model and data assimilation parameters based on noisy, potentially sparse observations of an underlying dynamical system, thereby streamlining the process to directly utilize observations. The framework can be used to learn nonlinear dynamics given linear observations of the state. As we will detail below, our framework generalizes existing learned data assimilation methods, including AD-EnKF (Chen et al., 2022) and AD-3DVar-K (Levine and Stuart, 2022). Furthermore, our framework leads to new methods that are efficacious for time-varying observation models or which require fewer computational resources. We formalize the problem setting in the next section.

1.1 Problem setting

Assume we collect observations $y_{1:T}$ derived from the following hidden Markov model

$$x_t^* = \mathcal{F}_{\theta_1^*}(x_{t-1}^*) + \tilde{Q}_{\theta_2^*} \xi_t, \quad \xi_t \sim N(0, I_{d_x}), \quad (1)$$

$$y_t = H_t x_t^* + \eta_t, \quad \eta_t \sim N(0, R_t), \quad (2)$$

$$x_0^* \sim p_0(x_0) \quad (3)$$

for time points $t = 1, \dots, T$, where $x_t^* \in \mathbb{R}^{d_x}$ is the true state vector at time t , $\mathcal{F}_{\theta_1^*}$ is the true dynamics map parameterized by true parameters θ_1^* , $Q_{\theta_2^*} := \tilde{Q}_{\theta_2^*} \tilde{Q}_{\theta_2^*}^\top \in \mathbb{R}^{d_x \times d_x}$ is the true forecast error covariance parameterized by θ_2^* , $y_t \in \mathbb{R}^{d_{y_t}}$ are noisy, potentially partial observations of x_t^* at time t , $H_t \in \mathbb{R}^{d_{y_t} \times d_x}$ is the time-varying, known linear observation matrix, $R_t \in \mathbb{R}^{d_{y_t} \times d_{y_t}}$ is the time-varying, known observation error covariance, and the initialization x_0^* is assumed to be unknown and drawn from a given prior distribution p_0 .

In this setting, we assume independence of x_0^* , $\xi_{1:T}$, and $\eta_{1:T}$.¹

In practice, the true dynamics mapping $\mathcal{F}_{\theta_1^*}$ is unknown, and instead, an imperfect model given by \mathcal{F}_{θ_1} , may be used, where θ_1 are the parameters of this imperfect dynamics mapping. We note that \mathcal{F}_{θ_1} may be structurally different from $\mathcal{F}_{\theta_1^*}$ (e.g., \mathcal{F}_{θ_1} could be a neural network with learnable parameters θ_1 , where these parameters do not have a one-to-one correspondence with the true governing parameters θ_1^*). This imperfect specification of the dynamics induces forecast errors ξ_t that are assumed to be Gaussian distributed as specified in (1).

One goal in this setup is to compute, for each $t = 1, \dots, T$, a state estimate x_t , referred to as an *analysis*, given previous and current observations $y_{1:t}$. This goal is achieved by the use of filtering algorithms in data assimilation, which often require specifying filtering parameters ϕ prior to deployment that control, for instance, the “trust” given to the forecasts compared to the observations. A key idea underlying our framework is that information obtained from computing these analyses via filtering can be used to update the imperfect forecast model’s parameters $\theta := \{\theta_1, \theta_2\}$ and the filtering parameters ϕ . Section 2 provides a general overview of our framework for joint learning of states, forecast parameters, and filtering parameters based on observations $y_{1:T}$, which can be applied to a broad class of scientific problems involving dynamical systems.

1.2 Contributions

Many prior works have explored utilizing partial, noisy observations to improve some aspect of the data assimilation pipeline, which we further detail in Section 3. Notable examples include the auto-differentiable ensemble Kalman filter (Chen et al., 2022, AD-EnKF) and the auto-differentiable 3DVar where the Kalman gain matrix is directly learned (Levine and Stuart, 2022, AD-3DVar-K), among others. Each method was developed separately with different settings in mind, some focusing more on learning the dynamics, some focusing more on

¹To explain our notation, $\xi_{1:T}$, as an example, denotes the time series of forecast model errors for time points $t = 1, \dots, T$.

learning filtering parameters, and others focusing on learning both aspects. **In this paper, we show that these goals can all be achieved under our general framework.**

Furthermore, armed with this approach, we can easily derive new methods that have important performance advantages over past work. We provide derivations of particular auto-differentiable filtering methods in Sections 2.1 and 2.2. Specifically, we derive the auto-differentiable 3DVar algorithm where the static forecast error covariance C is learned (AD-3DVar- C), as opposed to directly learning the Kalman gain K in AD-3DVar- K , which is outlined in Section 3. A benefit of AD-3DVar- C is that it can handle time-varying observation models salient to many application domains. Additionally, we derive the auto-differentiable ensemble 3DVar (AD-Ens3DVar), which serves as a computational middle ground between the lighter-weight AD-3DVar- C or - K and AD-EnKF for jointly learning dynamics and filtering parameters. Our contributions in this work are summarized as follows:

1. Formulate a general framework for co-learning of state, dynamics, and filtering algorithms and outline notable special cases of this framework (Section 2).
2. Propose two new algorithms: the auto-differentiable 3DVar algorithm (AD-3DVar- C) and the auto-differentiable hybrid ensemble 3DVar algorithm (AD-Ens3DVar) (Section 2).
3. Modify the existing auto-differentiable ensemble Kalman filter (AD-EnKF), developed in [Chen et al. \(2022\)](#) as an algorithm for co-learning states and dynamics, to additionally co-learn filtering parameters, namely the covariance inflation (Section 2).
4. Compare each particular case of our framework (i.e., AD-EnKF, AD-Ens3DVar, AD-3DVar- C) on illustrative examples spanning multiple domains (astronomy, atmospheric sciences, and population dynamics) that showcase advantages and disadvantages (Section 4).
5. Discuss settings where each example method derived from our framework may be useful based on performance in our examples in terms of accuracy, scalability, and computational efficiency (Section 5).

2 General learning framework

2.1 Filtering

In this work, we are particularly interested in learning from observations in a *filtering* setting, where the analysis at each time t , denoted x_t , is computed using observations up to the current time point, $\{y_{1:t}\}$. We consider a general class of filtering algorithms of the form

$$x_t^n = (I - \mathcal{K}_\phi(x_{t-1}^{1:N})H_t) \mathcal{M}_\theta(x_{t-1}^n) + \mathcal{K}_\phi(x_{t-1}^{1:N})\mathcal{Y}(y_t; R_t), \quad \text{for } t = 1, \dots, T, \quad (4)$$

where $\mathcal{M}_\theta(\cdot)$ is the forecast model parameterized by θ , $\mathcal{Y}(\cdot; R_t)$ is a function that incorporates observations and the observation error covariance R_t , $\mathcal{K}_\phi(\cdot)$ is a Kalman gain parameterized by ϕ that controls the “trust” given to the observations versus the forecast, n is the ensemble member index ($n = 1, \dots, N$), and $x_t^{1:N}$ denotes an ensemble comprising N state estimates at time t . For filtering algorithms that do not rely on an ensemble, $N = 1$, and we drop the superscripts from the notation. Throughout this paper, we refer to the map from the forecast $\mathcal{M}_\theta(x_{t-1}^n)$ and observations y_t to the analysis x_t^n for any time t as an *analysis step*. We also refer to a *filter* step as the map from the previous analysis x_{t-1}^n and observations y_t to the analysis x_t^n at some time t , where the computation for this mapping is given in (4).

Specific filtering algorithms can be expressed as equation (4) with particular choices of \mathcal{K}_ϕ , \mathcal{M}_θ , and \mathcal{Y} . The particular algorithms we consider in this paper are 3DVar ([Lorenç, 1986](#)) where the Kalman gain is fixed across time and parameterized by a background error covariance matrix C_ϕ (denoted as “3DVar- C ”), the ensemble Kalman filter ([Evensen, 1994](#), EnKF) where the time-evolving Kalman gain is defined in equations (6) and (8), and a hybrid approach, ensemble 3DVar ([Hamill and Snyder, 2000](#), Ens3DVar), where we define this hybrid covariance in (9). Table 1 shows how these three filtering algorithms can be expressed as particular instances of the abstract setup in equation (4).

Forecasting system \mathcal{M}_θ . The forecast system \mathcal{M}_θ consists of the forecasting model \mathcal{F}_{θ_1} and perturbations to the forecast model based on $\mathcal{N}(0, Q_{\theta_2})$ noise, where $\theta = \{\theta_1, \theta_2\}$. In (4), we define the forecast system as

$$\mathcal{M}_\theta(x_{t-1}^n) = \mathcal{F}_{\theta_1}(x_{t-1}^n) + s\tilde{Q}_{\theta_2}\xi_t^n, \quad (5)$$

where $s = 1$ if the user chooses to add forecast model perturbations and learn the covariance matrix Q_{θ_2} , and $s = 0$ if the user chooses to not add stochastic perturbations to the forecasting system. For each specific filtering algorithm we consider, we list this choice in Table 1. The decision to set $s = 1$ or $s = 0$ can be empirically motivated based on the choice of filtering method.

Alg.	$\mathcal{M}_\theta(x_{t-1}^n)$	$\mathcal{K}_\phi(x_{t-1}^{1:N})$	$\mathcal{Y}(\cdot; R_t)$	Ens. Size
3DVar- C	$\mathcal{F}_{\theta_1}(x_{t-1})$	$C_\phi H_t^\top (H_t C_\phi H_t^\top + R_t)^{-1}$ $C_\phi \in \mathbb{R}^{d_x \times d_x}$	y_t	1
EnKF	$\mathcal{F}_{\theta_1}(x_{t-1}^n) + \tilde{Q}_{\theta_2} \xi_t^n$ $\xi_t^n \sim \mathcal{N}(0, I_{d_x})$	$\hat{C}_t^{\theta, \phi} H_t^\top (H_t \hat{C}_t^{\theta, \phi} H_t^\top + R_t)^{-1}$ ($\hat{C}_t^{\theta, \phi}$ defined in (8))	$y_t + \gamma_t^n$ $\gamma_t^n \sim \mathcal{N}(0, R_t)$	N_{EnKF}
Ens3DVar	$\mathcal{F}_{\theta_1}(x_{t-1}^n) + \tilde{Q}_{\theta_2} \xi_t^n$ $\xi_t^n \sim \mathcal{N}(0, I_{d_x})$	$\tilde{C}_t^{\theta, \phi} H_t^\top (H_t \tilde{C}_t^{\theta, \phi} H_t^\top + R_t)^{-1}$ ($\tilde{C}_t^{\theta, \phi}$ defined in (9))	$y_t + \gamma_t^n$ $\gamma_t^n \sim \mathcal{N}(0, R_t)$	N_{Ens3DVar}

Table 1: Table of examples of named special cases of the general filtering algorithm defined in (4). We note that this list is not exhaustive.

Forecast covariance matrix $C_t^{\theta, \phi}$ in the Kalman gain $\mathcal{K}_\phi(\cdot)$. Each of the algorithms in Table 1 constructs the Kalman gain differently, and each requires specifying a forecast error covariance matrix $C_t^{\theta, \phi}$.

The 3DVar- C algorithm relies on a fixed-time covariance matrix C_ϕ parameterized by static parameters ϕ . To ensure that C_ϕ is a proper covariance matrix, we learn C_ϕ via a square matrix $B_\phi \in \mathbb{R}^{d_x \times d_x}$ such that $C_\phi = B_\phi B_\phi^\top$; this approach ensures that C_ϕ is a symmetric, positive semi-definite matrix. We provide a more detailed discussion with supplementary experiments regarding this choice in Appendix A.

For EnKF, an ensemble-based filtering algorithm, a time-dependent empirical forecast covariance matrix is computed as

$$\hat{C}_t^\theta = \frac{1}{N-1} \sum_{n=1}^N (\mathcal{M}_\theta(x_{t-1}^n) - \hat{m}_t^\theta)(\mathcal{M}_\theta(x_{t-1}^n) - \hat{m}_t^\theta)^\top, \quad (6)$$

which approximates the forecast covariance with a finite ensemble, with the empirical forecast mean given by

$$\hat{m}_t^\theta = \frac{1}{N} \sum_{n=1}^N \mathcal{M}_\theta(x_{t-1}^n). \quad (7)$$

When $N \ll d_x$, EnKF estimates of the state substantially improve when a covariance tapering matrix $\rho \in \mathbb{R}^{d_x \times d_x}$ is used, particularly in applications where the states have a spatial structure, such as the tapering matrix described in Gaspari and Cohn (1999). Moreover, the ensemble-based estimate of the forecast covariance matrix may exhibit under-dispersion, which can be combated with covariance inflation (Anderson, 2012). Combining the covariance inflation factor ϕ and the covariance tapering matrix ρ , the forecast covariance matrix used in EnKF filtering is

$$\hat{C}_t^{\theta, \phi} = (1 + \phi)(\rho \circ \hat{C}_t^\theta), \quad (8)$$

where \circ denotes the element-wise product.

In Ens3DVar, the forecast covariance matrix is specified to be a convex combination of a static 3DVar covariance matrix C_{ϕ_2} and a time-dependent EnKF matrix $\hat{C}_t^{\theta, \phi}$ computed in (8) with fixed covariance inflation and covariance tapering,² where the weighting is controlled by a scalar parameter $\phi_1 \in \mathbb{R}$,

$$\tilde{C}_t^{\theta, \phi} = (1 - \phi_1)C_{\phi_2} + \phi_1 \hat{C}_t^\theta, \quad (9)$$

where $\phi = \{\phi_1, \phi_2\}$.

We use a generalized notation $C_t^{\theta, \phi}$ for the forecast covariance matrix, where $C_t^{\theta, \phi} := \hat{C}_t^{\theta, \phi}$ for EnKF, $C_t^{\theta, \phi} := \tilde{C}_t^{\theta, \phi}$ for Ens3DVar, and $C_t^{\theta, \phi} := C_\phi$ for 3DVar. This general notation for the forecast covariance matrix $C_t^{\theta, \phi}$ is used throughout our description of auto-differentiable filtering algorithms in Section 2.2.

Observation perturbation \mathcal{Y} . For ensemble based methods, observation perturbation when computing innovations can help to mitigate the underestimation of the analysis error covariance, thereby discouraging ensemble collapse (Evensen, 1994; Houtekamer and Mitchell, 1998) and ensuring convergence to the Kalman filter with a large ensemble size in linear-Gaussian settings (Furrer and Bengtsson, 2007; Al-Ghathas and Sanz-Alonso, 2024). Therefore, the ensemble-based methods EnKF and Ens3DVar add a stochastic perturbation to the observations based on $\mathcal{N}(0, R_t)$ distributed noise. This step is omitted in the 3DVar algorithm, as shown in Table 1, since this algorithm does not rely on an ensemble for covariance estimation.

²The covariance inflation for the EnKF component of the Ens3DVar covariance can additionally be learned, but we do not pursue this task in our experiments.

Initial conditions $x_0^{1:N}$. The specification of the ensemble of initial conditions $x_0^{1:N}$ is problem specific, and the quality of this initial condition depends on how much is known about the state of the system at initialization. An initial condition x_0 can be specified as a “best guess” at $t = 0$, which could include interpolated observations y_0 . Alternatively, in the absence of detailed information at initialization, an arbitrary initialization can be specified, in which case the spin-up time for the filter to produce reasonable analyses increases. An ensemble can then be created by perturbing this initial condition with random noise distributed with initial covariance C_0 , which can be arbitrarily specified or based on apriori knowledge of the system.

2.2 Auto-differentiable filtering

With the filtering algorithm defined in (4), we can learn the dynamics parameters θ and filtering parameters ϕ via auto-differentiation, then estimate states by using a filtering algorithm with these learned parameters. Algorithm 1 specifies this joint learning and filtering task. This algorithm outlines a three-step procedure where (a) gradient information with respect to the learnable parameters θ and ϕ is tracked through the filtering algorithm, (b) a theoretically motivated loss function computes the discrepancy in the observations and the analysis means, and (c) gradient information computed based on our choice of loss function informs gradient descent on the learnable parameters. Steps (a)-(c) are repeated until convergence of the parameters θ and ϕ . At each iteration k of the optimization, state estimates $x_{1:T}^{1:N,(k)}$ are constructed using the filtering algorithm in (4). The final state estimates $x_{1:T}^{1:N}$ are constructed by filtering with the converged $\hat{\theta}$ and $\hat{\phi}$.

Algorithm 1 Auto-differentiable filtering

Input: Initial time samples $x_0^{1:N}$ with ensemble size N , observations $y_{1:T}$, initialized forecast model $\mathcal{M}_{\theta^{(0)}}(\cdot)$, initialized Kalman gain $\mathcal{K}_{\phi^{(0)}}(\cdot)$, observation perturbation model $\mathcal{Y}(\cdot; R_{1:T})$, observation matrices $H_{1:T}$
while θ, ϕ are not converging: **do**
 $x_{1:T}^{1:N,(k)} = \text{Filter}(x_0^{1:N}, y_{1:T}; \mathcal{M}_{\theta^{(k)}}(\cdot), \mathcal{K}_{\phi^{(k)}}(\cdot), \mathcal{Y}(\cdot; R_{1:T}), H_{1:T})$ ▷ Eq. (4)
 $\mathcal{L}(\theta^{(k)}, \phi^{(k)}) = -\sum_{t=1}^T \log \mathcal{N}(y_t; H_t \hat{m}_t^{\theta^{(k)}}, H_t C_t^{\theta^{(k)}, \phi^{(k)}} H_t^\top + R_t)$
 $\theta^{(k+1)} = \theta^{(k)} - \alpha_{1,k} \nabla_{\theta} \mathcal{L}(\theta^{(k)}, \phi^{(k)})$
 $\phi^{(k+1)} = \phi^{(k)} - \alpha_{2,k} \nabla_{\phi} \mathcal{L}(\theta^{(k)}, \phi^{(k)})$
 $k \leftarrow k + 1$
end while
Output: Analysis estimates $x_{1:T}^{1:N}$, learned forecast parameters $\hat{\theta}$, learned analysis parameters $\hat{\phi}$

Algorithm 1 includes prespecified optimization hyperparameters $\alpha_{1,k}$ and $\alpha_{2,k}$, which correspond to the learning rates for θ and ϕ , respectively, at iteration k . For each iteration of the algorithm, the same set of initial conditions $x_0^{1:N}$ is used.

Loss function. We define our loss function $\mathcal{L}(\theta, \phi)$ using similar motivation as in [Chen et al. \(2022\)](#) and [Bach et al. \(2025b\)](#) (Theorem 8.12). Specifically, we aim to maximize the log-likelihood function of the observations $p(y_{1:T}|\theta, \phi)$ with respect to the parameters θ and ϕ , which can be written as

$$\log p(y_{1:T}|\theta, \phi) = \sum_{t=1}^T \log p(y_t|y_{1:t-1}, \theta, \phi) \quad (10)$$

based on the law of total probability, setting $y_{1:0} = 0$ by convention. Using the observation process model, $y_t = H_t x_t + \eta_t$, we can create a Gaussian ansatz of the distribution $p(y_t|y_{1:t-1}, \theta, \phi)$ by estimating the corresponding mean and variance as follows:

$$\mathbb{E}(y_t|y_{1:t-1}, \theta, \phi) = \mathbb{E}(H_t x_t + \eta_t|y_{1:t-1}, \theta, \phi) \approx H_t \hat{m}_t^\theta, \quad (11)$$

and

$$\text{Cov}(y_t|y_{1:t-1}, \theta, \phi) = \text{Cov}(H_t x_t + \eta_t|y_{1:t-1}, \theta, \phi) \approx H_t C_t^{\theta, \phi} H_t^\top + R_t := S_t, \quad (12)$$

where \hat{m}_t^θ and $C_t^{\theta, \phi}$ are the estimated forecast mean and forecast error covariance at time t , respectively. These estimated components allow us to construct the following Gaussian approximation

$$\log p(y_{1:T}|\theta, \phi) \approx \sum_{t=1}^T \log \mathcal{N}(y_t; H_t \hat{m}_t^\theta, H_t C_t^{\theta, \phi} H_t^\top + R_t) =: -\mathcal{L}(\theta, \phi), \quad (13)$$

which can be more explicitly written as

$$\mathcal{L}(\theta, \phi) := -\sum_{t=1}^T \left[-\frac{1}{2} \log \det(S_t) - \frac{1}{2} \|y_t - H_t \hat{m}_t^\theta\|_{S_t}^2 \right], \quad (14)$$

where $\mathcal{L}(\theta, \phi) \propto \log p(y_{1:T}|\theta, \phi)$ up to an additive constant independent of θ and ϕ . This function $\mathcal{L}(\theta, \phi)$ is our loss function.

Equation (14) provides a loss that allows us to (approximately) maximize the likelihood of our observations with respect to the forecast parameters θ and analysis parameters ϕ across the entire time series. We note that this derivation relies on the linearity of H_t . Moreover, the accuracy of the approximations in (13) is contingent on the forecast distribution being well approximated with a Gaussian $\mathcal{N}(\hat{m}_t^\theta, C_t^{\theta, \phi})$ distribution.

Optimization. To (approximately) maximize $p(y_{1:T}|\theta, \phi)$ with respect to parameters θ and ϕ , we consider the optimization problem

$$\{\hat{\theta}, \hat{\phi}\} = \operatorname{argmin}_{\theta, \phi} \mathcal{L}(\theta, \phi). \quad (15)$$

The gradient descent steps in Algorithm 1 seek to solve this problem via gradient-based optimization.

As is developed in Chen et al. (2022) for AD-EnKF, we similarly implement a training procedure for Algorithm 1 inspired by truncated backpropagation through time (TBPTT) (Sutskever et al., 2014). With this approach, updates to θ and ϕ are applied after iterating through a subsequence of L assimilation steps, where $L \ll T$. This procedure results in $\lceil T/L \rceil$ gradient updates per epoch,³ which can avoid the problem of vanishing or exploding gradients that can occur when auto-regressively applying learned models to time series data over long time horizons. The modification to Algorithm 1 to account for TBPTT is detailed in Appendix B.

We emphasize that while filtering is an *online* algorithm, meaning that the filtering algorithms can be deployed as soon as new observations arrive, we formulate the optimization problem for learning θ and ϕ in an *offline* fashion, meaning the observations need to be collected in a batch, after which Algorithm 1 is deployed.

A note on necessary conditions. We now emphasize a few necessary conditions for a method to fall within the class of auto-differentiable filtering algorithms that we define here. First and foremost, the algorithm used to compute state estimates $x_{1:T}$ must depend on current and past observations, so x_t must only be informed by observations $y_{1:t}$. Second, we emphasize that the specifications of the components in (4) are flexible enough to handle time-varying H_t in order to encompass a wide range of applied settings. Lastly, the filtering algorithm must provide a means to estimate the covariance in (12) to compute the theoretically-motivated loss function in (14). If a particular filtering algorithm does not satisfy any one of these criteria, it is not considered to be a part of this framework.

2.3 Computational considerations

In this section, we provide computational considerations for this framework, and particularly emphasize the computational and memory differences for learning via ensemble-based filtering algorithms (e.g., EnKF and Ens3DVar) compared to ensemble-free filtering algorithms (e.g., 3DVar). We discuss the computational complexity in terms of particular filtering algorithms themselves since the filtering algorithm is the main driver of computational cost; the cost of auto-differentiation is proportional to the computational complexity of the filtering process up to a constant factor (Griewank and Walther, 2008; Baydin et al., 2018).

Computational costs. The computational costs of the forecast and analysis in one filtering step is given in Table 2 for 3DVar- C , EnKF, and Ens3DVar. In 3DVar- C with our specification of $C_\phi = B_\phi B_\phi^\top$, where $B_\phi \in \mathbb{R}^{d_x \times d_x}$ and H_t is linear, the computational cost of a 3DVar- C analysis step is $\mathcal{O}(d_y^3 + d_y^2 d_x + d_y d_x^2)$. If $H_t \equiv H$, meaning the observed states remain constant across time, the Kalman gain $C_\phi H^\top (H C_\phi H^\top + R)^{-1}$ only needs to be computed once per fixed ϕ , after which the computational cost for each 3DVar- C analysis step becomes $\mathcal{O}(d_y d_x)$. Denoting by $c_{\mathcal{F}}$ the computational cost of a forecast from \mathcal{F}_{θ_1} , since 3DVar- C relies on a single particle, the cost of the forward pass would be $\mathcal{O}(c_{\mathcal{F}})$.

As noted in Mandel (2006), the computational complexity of a straight-forward implementation of an analysis step of EnKF is $\mathcal{O}(d_y^3 + d_y^2 N + d_y N^2 + d_x N^2)$, where the dominating term depends on the relative values of d_x , N , and d_y , but in many applications, $d_x \gg d_y \gg N$. For the computational cost of alternative implementations of the EnKF analysis step, we refer to Tippett et al. (2003). The computational cost for forecasting the ensemble of N total members is $\mathcal{O}(N c_{\mathcal{F}})$.

For Ens3DVar, the computational cost depends on the dominating terms of 3DVar- C and EnKF, which gives $\mathcal{O}(d_y^3 + d_y^2 d_x + d_x^2 d_y)$ assuming that $N \ll d_y$. For the forecast step, Ens3DVar incurs a computational cost of $\mathcal{O}(N c_{\mathcal{F}})$ for propagating the ensemble of size N with the forecast model.

In many applications, the cost of a filtering step is usually dominated by the computational cost of evaluating the forward model, which is amplified by a factor of N for ensemble-based methods when performed serially. However, this cost can be reduced via parallelization.

³In the context of our offline auto-differentiable filtering framework, an epoch refers to filtering through and updating learnable parameters for all time points in the training data.

	Forecast cost	Analysis cost
3DVar- C	$c_{\mathcal{F}}$	$\mathcal{O}(d_y^3 + d_x^2 d_y + d_y^2 d_x)$
EnKF	$N c_{\mathcal{F}}$	$\mathcal{O}(d_y^3 + d_y^2 N + d_y N^2 + d_x N^2)$
Ens3DVar	$N c_{\mathcal{F}}$	$\mathcal{O}(d_y^3 + d_x^2 d_y + d_y^2 d_x)$

Table 2: Table of computational costs for the forecast and analysis in one filtering step for straight-forward implementations of the algorithms 3DVar- C , EnKF, and Ens3DVar, where we assume that $N \ll d_y$ for Ens3DVar.

Memory costs. One aspect of auto-differentiable filtering that substantially impacts the memory footprint, as additionally noted in [Chen et al. \(2022\)](#), is the length of the time series T , or L if training with TBPTT. The computational graph needs to be stored as the filter sequentially processes data, and memory can only be cleared after backpropagating through the time series (for T steps, or L steps if using TBPTT) and updating the learnable parameters. When using TBPTT, choices of large L can lead to substantial memory consumption; on the other hand, too small L can bias training by ignoring potentially important longer-range dependencies ([Aicher et al., 2020](#)). This choice requires empirical tuning.

For ensemble-based methods, another choice that can substantially impact the memory footprint is the number of ensemble members N . The memory footprint of these ensemble-based methods increases by a factor of N compared to single-particle filters, but this increased memory footprint as N increases generally comes with the benefit of better learning, as shown for AD-EnKF in [Chen et al. \(2022\)](#). For high-dimensional systems, storing large ensembles, tracking the trajectories through a long time sequence, and backpropagating to update the learnable parameters can easily exceed memory limits if memory is not precisely considered.

3 Related work

There is a vast body of literature developed in recent years regarding machine learning in data assimilation. [Bach et al. \(2025b\)](#) provides a thorough review of the current state of machine learning for inverse problems and data assimilation. We highlight particular works related to our learning goal, including papers that aim to learn forecast model parameters, learn analysis parameters, or jointly learn forecast and analysis parameters from noisy, potentially partial observations.

Learning forecast parameters from observations. Numerous previous works have proposed various approaches to updating a forecast model based on observations via data assimilation: to name a few, [Brajard et al. \(2020\)](#) and [Chen et al. \(2022\)](#) (AD-EnKF) use an ensemble Kalman filter and auto-differentiation to learn a surrogate model; [Gottwald and Reich \(2021\)](#) learns a forecast model based on sparse information using a random feature map and EnKF data assimilation; [Bocquet et al. \(2021\)](#) studies joint estimation of dynamics and states via EnKF, comparing online and offline learning with sparse observations; and [Farchi et al. \(2021\)](#) corrects model error via 4DVar data assimilation. Additionally, [Wang and Jiang \(2025\)](#) presents EnKF and particle filter variants that allow for forecast parameter learning via formulating the problem as a discrete time Markov decision process from a reinforcement learning perspective. [Chen et al. \(2023\)](#) proposes to learn a reduced order model that performs data assimilation in a latent space, where a decoder then maps latent states back to the original state space, thereby learning a low-dimensional, computationally efficient filter. Though less frequently used, auto-differentiable particle filters have also been developed for learning forecast components, such as in [Ścibior and Wood \(2021\)](#); we refer to [Chen and Li \(2025\)](#) for a review of these methods.

Learning analysis parameters from observations. Recent works have explored learning portions of the analysis step in data assimilation methods while keeping the dynamics mapping fixed. [Melinc and Zaplotnik \(2024\)](#) learns an autoencoder to perform a 3DVar update in a reduced space, thereby allowing for faster computation. [Bach et al. \(2025a\)](#) learns a Kalman gain for variational filtering problems. [Lu \(2025\)](#) uses machine learning to learn improved localized error covariance matrices within EnKF. [Revach et al. \(2022\)](#) learns a Kalman-type update from partial, noisy observations that does not rely on potentially limiting assumptions of Gaussian error statistics that are assumed in traditional data assimilation. [Bach et al. \(2026\)](#) learns ensemble filtering algorithms via a mean-field state-space formulation of filtering. Methods that retain the traditional Gaussianity assumptions on the error statistics and aim to learn components of the analysis could be integrated into the framework we propose in this work.

Joint learning of forecast and analysis parameters from observations. [Chinellato and Marcuzzi \(2025\)](#) propose an algorithm based on the Kalman filter, where Kalman gain-type matrices are learned for each filter step

along with the dynamics mapping. Additionally, that work explores regularization on the dynamics mapping via SINDy (Brunton et al., 2016). Lunderman et al. (2021) jointly learns analysis and forecast parameters via derivative-free global Bayesian optimization for offline learning from observations. Another algorithm that achieves the goal of jointly learning forecast and analysis parameters is Levine and Stuart (2022). We provide a detailed discussion of this method below.

A comparable algorithm: AD-3DVar- K . We now describe in detail a method we will refer to as AD-3DVar- K that is proposed in Levine and Stuart (2022). This work aims to learn forecast model errors via auto-differentiation through a 3DVar-type algorithm. Since this algorithm achieves the same overarching goals as our general learning framework (learning states, forecast and filtering parameters), we include this method in our experimental results as a point of comparison. However, this method departs from the framework we outline in Section 2 in nontrivial ways, which we detail here. Most notably, this method is unable to handle observations that come from a time-varying H_t , which limits its use in many practical settings.

AD-3DVar- K specifies the 3DVar filtering algorithm (denoted as 3DVar- K in this work) as

$$x_t = (I - K_\phi H) \mathcal{F}_{\theta_1}(x_{t-1}) + K_\phi y_t, \quad (16)$$

where $K_\phi \in \mathbb{R}^{d_y \times d_x}$ is a Kalman gain matrix directly parameterized by ϕ (i.e., this matrix is not computed using information in H , R or some choice of C). We also note the subscript t on d_y and H has been deliberately dropped because this method only applies to settings where the observation matrix H is fixed across the entire assimilation window.

AD-3DVar- K outlines an algorithm of the same form as Algorithm 1, except a key distinction is in the choice of loss function $\mathcal{L}(\theta, \phi)$. Since the Kalman gain matrix K_ϕ is learned directly, the forecast covariance in the observation space ($H C^{\theta, \phi} H^\top + R$) is not directly available, and therefore, the loss derived in (14) cannot be directly computed. Instead, the loss is defined as

$$\mathcal{L}_{3\text{DVar-}K}(\theta, \phi) := \frac{1}{T} \sum_{t=1}^T \|y_t - H \mathcal{F}_{\theta_1}(x_{t-1})\|^2, \quad (17)$$

which implicitly assumes that the residuals across all components carry equal variance, therefore that $H C H^\top + R$ is a multiple of the identity matrix. Gradient information is similarly tracked with respect to θ and ϕ throughout the time series, where $\theta := \theta_1$, and gradient descent is performed to minimize this loss. Though ϕ does not explicitly appear in (17), ϕ implicitly appears in x_{t-1} since it is constructed using (16). The optimization problem can be written as

$$\{\hat{\theta}, \hat{\phi}\} = \operatorname{argmin}_{\theta, \phi} \mathcal{L}_{3\text{DVar-}K}(\theta, \phi), \quad (18)$$

where gradient-descent optimization steps of a similar form: $\theta^{(k+1)} = \theta^{(k)} - \alpha_{1,k} \nabla_{\theta} \mathcal{L}(\theta^{(k)}, \phi^{(k)})$ and $\phi^{(k+1)} = \phi^{(k)} - \alpha_{1,k} \nabla_{\phi} \mathcal{L}(\theta^{(k)}, \phi^{(k)})$ for iterations $k = 1, \dots$ are taken until convergence. Once convergence is achieved, state estimates $x_{1:T}$ are computed by filtering with the learned $\hat{\theta}$ and $\hat{\phi}$ parameters.

We now briefly discuss the computational demands of this approach compared to the particular methods discussed in Section 2.3 that fall into our framework. Among the particular methods mentioned, AD-3DVar- K is the most computationally- and memory-efficient. Since AD-3DVar- K is ensemble-free and directly learns a matrix $K_\phi \in \mathbb{R}^{d_y \times d_x}$, this approach avoids the computationally intensive $d_y \times d_y$ matrix inversion in AD-3DVar- C at each time point t , and additionally only stores the Kalman gain matrix, which contains $(d_x - d_y)d_x$ fewer elements than a dense C_ϕ matrix for $d_y \ll d_x$. The overall computational complexity of each analysis step is $\mathcal{O}(d_y d_x)$ and $\mathcal{O}(c_{\mathcal{F}})$ for each forecast.

4 Experiments

Our experiments aim to explore our framework across multiple scientific settings with different learning goals for the forecast component, namely learning residual neural networks and parameter estimation to improve forecast performance. We evaluate the forecast performance of $\hat{\theta}_1$ and the filtering performance using the learned $\hat{\theta}$ and $\hat{\phi}$ across four methods: AD-3DVar- C , AD-3DVar- K , AD-EnKF modified to additionally learn the covariance inflation factor,⁴ and AD-Ens3DVar. Section 4.1, motivated by a simplified problem in astrodynamics, explores learning from observations of a partially observed linear dynamical system. Experimenting on a system with linear dynamics and linear observations allows us to compare how well each method approximates the optimal solution given by the Kalman filter when using the true forecast model parameters. Section 4.2, motivated by applications in the atmospheric sciences, illustrates learning a residual neural network in a nonlinear dynamics

⁴Learning the covariance inflation factor in (8) corresponds to the modification we make to the algorithm presented in Chen et al. (2022); therefore, in our experiments, we label this approach as ‘‘AD-EnKF (Modified).’’ The tapering matrix ρ in (8) could additionally be learned, but doing so can be computationally expensive. We further discuss this point in Appendix C.

setting with a *static* observation matrix H . Lastly, Section 4.3, motivated by problems in population dynamics, illustrates that methods that fall under our framework are able to learn from partial observations where the observation matrix and its dimension may vary across time.

For all experiments, we visualize the performance of the learned forecast model parameters $\hat{\theta}_1$ across a variety of values of the problem (e.g., error level σ_0^2 in the initialized model, state observability ratio d_y/d_x , training data size T , etc.).⁵ We additionally evaluate the performance of the learned components $\hat{\theta}$ and $\hat{\phi}$ in a filtering task for assimilating unseen observation data for each algorithm. Evaluation metrics used in these experiments are defined in Appendix E, and additional training details for each example, including a discussion of hyperparameter tuning for the optimization learning rates, are listed in Appendix F. In each experiment, the forecast model \mathcal{F}_{θ_1} in (1) corresponds to the Δt -flow of each considered differential equation, where Δt represents the time between observations. Additionally, we experiment on deterministic dynamical systems, where the true forecast error parameters are $Q_{\theta_2^*} = \mathbf{0}_{d_x \times d_x}$ when forecasting with the true mapping $\mathcal{F}_{\theta_1^*}$.

4.1 Astrodynamics: Clohessy–Wiltshire equations

The Clohessy-Wiltshire equations (Clohessy and Wiltshire, 1960), built upon work in Hill (1878), are a simplified model for orbital motion, where a “target” object is in a circular orbit and a “chaser” object is in either an elliptical or circular orbit. These equations are the basis for planning orbital rendezvous of a spacecraft with another object. The equations are

$$\frac{d^2 x_1}{dt^2} = 3\theta^2 x_1 + 2\theta \frac{dx_2}{dt}, \quad (19)$$

$$\frac{d^2 x_2}{dt^2} = -2\theta \frac{dx_1}{dt}, \quad (20)$$

$$\frac{d^2 x_3}{dt^2} = -\theta^2 x_3, \quad (21)$$

where $\theta_1 \in \mathbb{R}_+$ is the orbital rate of the target, $[x_1, x_2, x_3]$ is the position vector, $[\frac{dx_1}{dt}, \frac{dx_2}{dt}, \frac{dx_3}{dt}]$ is the velocity vector, and $[\frac{d^2 x_1}{dt^2}, \frac{d^2 x_2}{dt^2}, \frac{d^2 x_3}{dt^2}]$ is the acceleration vector of the chaser object relative to the target. The goal is to construct estimates of a state vector $x = [x_1, x_2, x_3, \frac{dx_1}{dt}, \frac{dx_2}{dt}, \frac{dx_3}{dt}]$ across time.⁶

4.1.1 Learning task

This experiment is formulated as a simple parameter estimation problem where the goal is to recover a true scalar $\theta_1^* := 0.0013$ based on only noisily observing the position vector $[x_1, x_2, x_3]$ across time, therefore $H = I_{3 \times 6}$ is a time-independent identity matrix with rows deleted that correspond to the velocity state components. Initial guesses $\theta_1^{(0)}$ are sampled from $\mathcal{N}(\theta_1^*, \sigma_0^2)$, where $\sigma_0^2 \in \mathbb{R}$ controls the variance of the noise for our initial guess for the parameter. This σ_0^2 parameter is varied in some experiments.

4.1.2 Results

Data generation and training details for this example can be found in Appendix F.1. Optimization hyperparameters were tuned for each simulation and parameter value across the $J = 10$ independent simulated initial models. The time step between observations for this example is $\Delta t = 10$.

Performance in learning forecast parameters $\hat{\theta}_1$. Figure 1 shows the forecast performance using the estimated $\hat{\theta}_1$ across various parameter settings, namely the noise level σ_0^2 in the initialized $\theta_1^{(0)}$ and the observation noise variance. The ensemble-based methods AD-EnKF and AD-Ens3DVar achieve low MAE errors in recovering the true parameter θ_1^* across all choices of R and σ_0^2 . On the other hand, the AD-3DVar algorithms achieve less significant improvements to the initial imperfect $\theta_1^{(0)}$, as evidenced by the fact that the quantile spread of these two methods overlap with the quantile spread of the collection of initialized models.

Filtering performance using the learned $\hat{\theta}$ and $\hat{\phi}$. Figure 2 visualizes the filtering performance using the learned forecast parameters $\hat{\theta}$ and filtering parameters $\hat{\phi}$ across each of the four methods in the setting where $H = I_{3 \times 6}$, $\sigma_0^2 = 0.03$, and $R = 0.1I_{3 \times 3}$ for one randomly initialized model. The ensemble-based methods AD-EnKF and AD-Ens3DVar provide the best filtering performance, and show significantly more precise estimation of the unobserved velocity state components $\frac{dx_1}{dt}$ and $\frac{dx_3}{dt}$ compared to both AD-3DVar- C and AD-3DVar- K .

⁵An additional comparison where the ensemble sizes N varies for the methods AD-EnKF (Modified) and AD-Ens3DVar is provided in Appendix D.

⁶Here and in the following examples, x_i denotes the i -th component of the state vector x rather than the assimilation time.

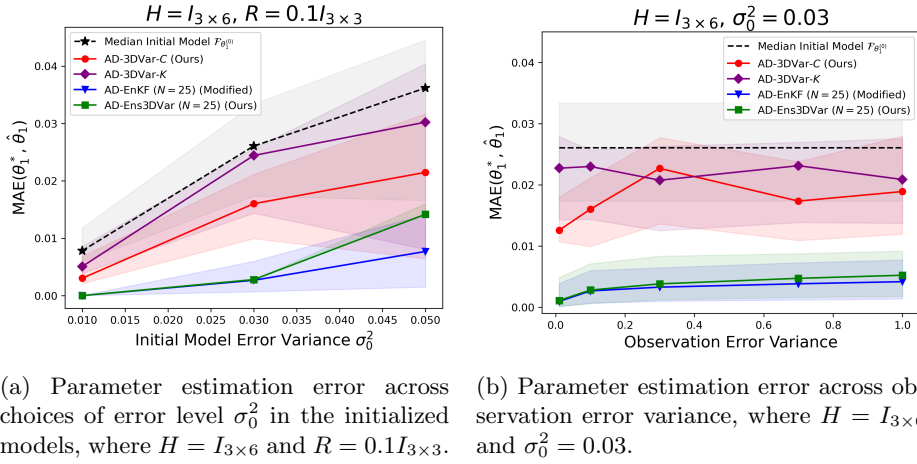


Figure 1: Clohessy-Wiltshire parameter estimation (Section 4.1). Parameter estimation error of the learned forecast parameter $\hat{\theta}_1$ compared to the ground truth parameter $\theta_1^* = 0.0013$ across choices of σ_0^2 and variance on the diagonals of R . The shaded regions correspond to the 0.25 and 0.75 quantiles of errors across 10 independent simulations. We additionally plot the median error for the initialized parameters $\{\theta_{1,j}^{(0)}\}_{j=1}^J$ for $j = 1, \dots, J = 10$ in the dashed black line (c) representing the errors in the absence of any learning, and the gray region corresponds to the 0.25 and 0.75 quantiles of test forecast RMSEs across these 10 initialized models.

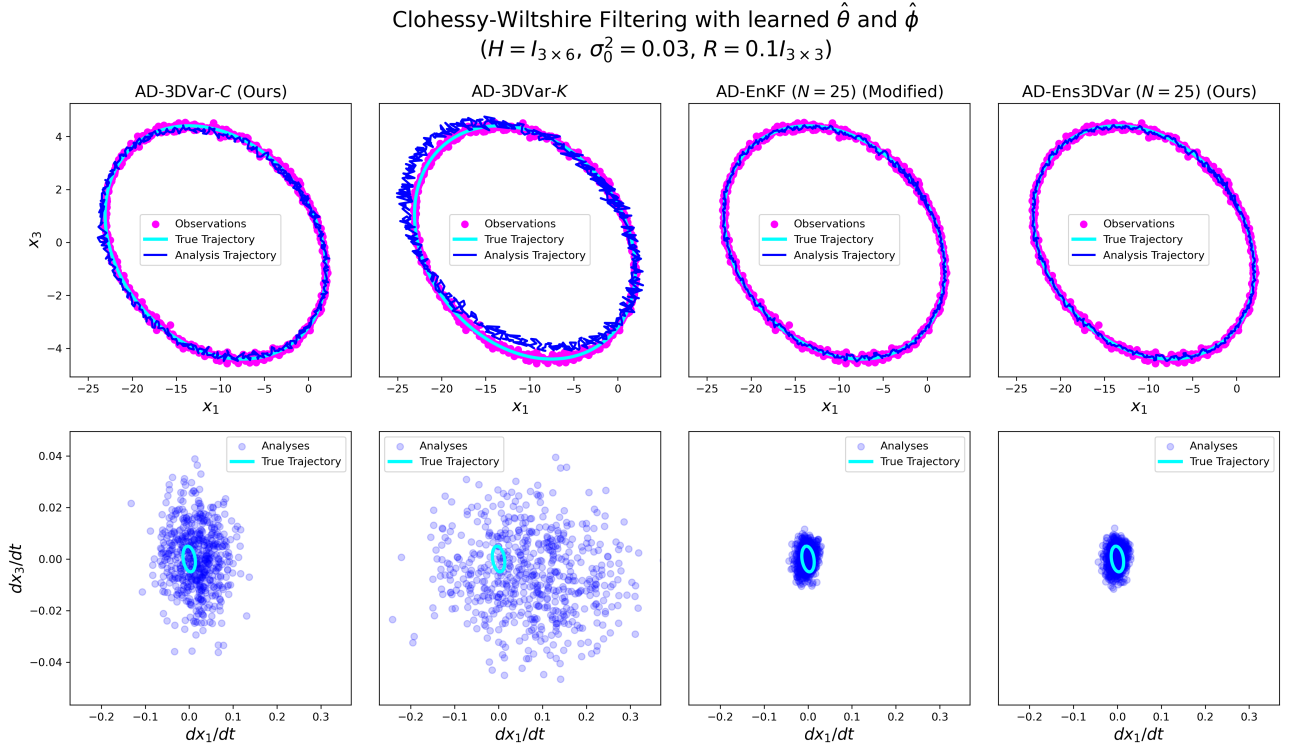


Figure 2: Clohessy-Wiltshire filtering (Section 4.1). Visualization of observations, true trajectories, and estimated positions for x_1 and x_3 , and velocities $\frac{dx_1}{dt}$ and $\frac{dx_3}{dt}$ across each of the four filtering methods using the learned forecast parameters $\hat{\theta}$ and learned filtering parameters $\hat{\phi}$, evaluated on test data. In this example, the observation noise is fixed at $R = 0.1I_{d_y \times d_y}$, and the variance of the initialization of $\theta_1^{(0)}$ is fixed at $\sigma_0^2 = 0.03$.

AD-3DVar- C provides an accurate estimate of the observed components but struggles more to recover the velocity components. AD-3DVar- K , on the other hand, most notably struggles to estimate the states for both the position and velocity components. An additional visualization similar to Figure 2 for positions x_2 and x_3 and velocities $\frac{dx_2}{dt}$ and $\frac{dx_3}{dt}$ across methods is shown in Figure 13 in Appendix F.1.3, and similar conclusions are derived from this figure. An evaluation of the learned covariance inflation factor in AD-EnKF (Modified) and the learned covariance mixing parameter in AD-Ens3DVar for the Clohessy-Wiltshire equations can be found in Figure 12 in Appendix F.

Estimation of the true forecast log-likelihood. Since our dynamics mapping and our observation function $H_t \equiv H$ are both linear, the filtering distribution for this problem is given by the Kalman filter (Kalman, 1960). We utilize this fact to evaluate how well EnKF, Ens3DVar, and 3DVar with their corresponding learned parameters $\hat{\theta}$ and $\hat{\phi}$ estimate the true forecast log-likelihood given by the Kalman filter (Eq. (10)) evaluated at observations. This comparison shows how close each method is to optimal in a simple linear setting. We provide implementation details of the Kalman filter in this setting in Appendix F.1.4. Figure 3 shows the approximation to the true log-likelihood based on 3DVar, EnKF, and Ens3DVar given the respective learned $\hat{\theta}$ and $\hat{\phi}$ from AD-3DVar- C , AD-EnKF, and AD-Ens3DVar compared to the log-likelihood given by the Kalman filter. We note that AD-3DVar- K does not appear in this comparison since learning K does not allow us to directly construct this log-likelihood. Consistent with the results presented in Figures 1 and 2, the ensemble-based approaches AD-EnKF and AD-Ens3DVar provide a better approximation to the true forecast log-likelihood, and AD-3DVar- C provides a much noisier approximation to this quantity. Both components of this log-likelihood ($-\frac{1}{2} \log \det S_t$ and $-\frac{1}{2} \|y_t - H_t \hat{m}_t^\theta\|_{S_t}^2$) are individually visualized in Figure 14 and discussed in Appendix F.1.4.

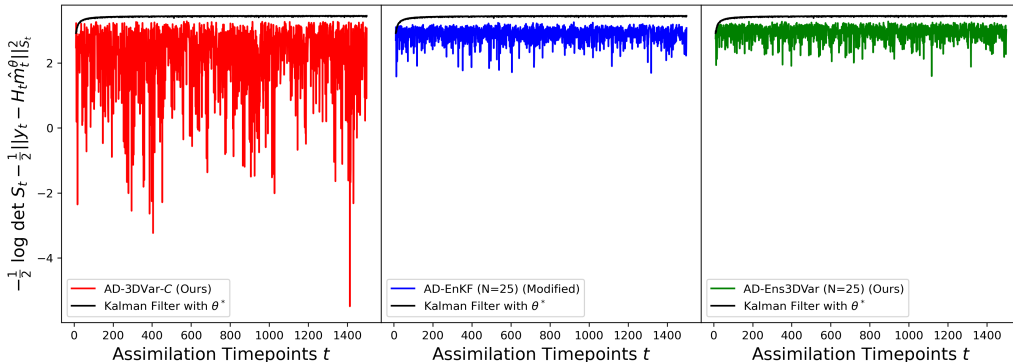


Figure 3: Clohessy-Wiltshire data log-likelihood (Section 4.1). Plots of the forecast log-likelihood evaluated at observations from (10) for assimilating test observations into filters parameterized by the learned forecast parameters $\hat{\theta}$ and $\hat{\phi}$ learned from AD-3DVar- C , AD-EnKF ($N = 25$), and AD-Ens3DVar ($N = 25$). The algorithm used for filtering corresponds to the algorithm used in the learning task (i.e., EnKF is used as the filter with the learned parameters from AD-EnKF). The log-likelihood from the optimal solution to the filtering task, the Kalman filter (detailed in Algorithm 3) using the true forecast parameters θ^* , is shown in each plot as a comparison.

4.2 Atmospheric dynamics: Lorenz-96

Next, we perform experiments on the Lorenz-96 system (Lorenz, 1995)

$$\frac{dx_i}{dt} = (x_{i+1} - x_{i-2})x_{i-1} - x_i + F, \quad (22)$$

where $x_i \in \mathbb{R}$, $i = 1, \dots, d_x$ and F is a forcing term that controls the chaotic behavior of the system, and we set $F = 8$ to induce chaos. We additionally impose the standard periodic boundary conditions $x_{-1} := x_{d_x-1}$, $x_{-2} := x_{d_x-2}$, and $x_{d_x} := x_0$ where $d_x \geq 4$. The state vector $x_t \in \mathbb{R}^{d_x}$ corresponds to the solution to (22) at time $t\Delta t$, where Δt is the time between observations; we recall the convention we use in the examples, where x_i denotes the i -th component of the state vector $x \in \mathbb{R}^{d_x}$. This system is used as a testbed for data assimilation methods for atmospheric applications due to its observed chaotic behavior for certain parameterizations and its simplified approximation of nonlinear advection in weather patterns.

4.2.1 Learning task

For this example, we consider learning a neural network residual correction to an imperfect model \mathcal{F}_0 . The forecast model is parameterized as

$$\mathcal{F}_{\theta_1} := \mathcal{F}_0 + \mathcal{G}_{\theta_1}, \quad (23)$$

where \mathcal{G}_{θ_1} is a residual neural network parameterized by learnable weights θ_1 that aim to correct \mathcal{F}_0 's predictions. This \mathcal{F}_{θ_1} model computes forecasts $\hat{x}_t = \mathcal{F}_0(x_{t-1}) + \mathcal{G}_{\theta_1}(x_{t-1})$ for any time t , where $x_t \in \mathbb{R}^{d_x}$.

The residual structure of \mathcal{F}_{θ_1} is motivated by its practical use in many settings where the aim is to blend physics-based and data-driven models. For example, \mathcal{F}_0 can be simplified partial differential equations, and \mathcal{G}_{θ_1} can be a learnable neural network, which is common to the task of learning closure models (Sanderse et al., 2025).

Imperfect initial model \mathcal{F}_0 . Given our goal to learn a model correction as specified in (23), we first describe how we create imperfect initial models based on the Lorenz-96 system. To create an imperfect model \mathcal{F}_0 , we take inspiration from experiments in (Chen et al., 2022) and similarly define a basis consisting of 2-degree polynomials of the terms $[x_{i-2}, x_{i-1}, x_i, x_{i+1}, x_{i+2}]$ to construct a differential equation of the form

$$\begin{aligned} \mathcal{F}_\beta^{(i)}(x) = \frac{dx_i}{dt} = & [1, x_{i-2}, x_{i-1}, x_i, x_{i+1}, x_{i+2}, \\ & x_{i-2}^2, x_{i-1}^2, x_i^2, x_{i+1}^2, x_{i+2}^2, \\ & x_{i-2}x_{i-1}, x_{i-1}x_i, x_ix_{i+1}, x_{i+1}x_{i+2}, x_{i-2}x_i, x_{i-1}x_{i+1}, x_ix_{i+2}]\beta, \end{aligned} \quad (24)$$

for $i = 1, \dots, d_x$, where $\beta \in \mathbb{R}^{18}$ are the coefficients of the basis polynomials. Equation (22) can be represented as (24) if $\beta = \beta^*$, where $\beta^* \in \mathbb{R}^{18}$ and $\beta_0^* = 8$, $\beta_3^* = -1$, $\beta_{11}^* = -1$, $\beta_{16}^* = 1$, $\beta_m^* = 0$ otherwise, and m indexes the 18 total coefficients in the 2-degree polynomial library for the collection of terms $[x_{i-2}, x_{i-1}, x_i, x_{i+1}, x_{i+2}]$.

We use the ground truth coefficients β^* of the Lorenz-96 system to randomly generate noisily perturbed coefficients β that are centered around the true parameter. More concretely, we specify \mathcal{F}_0 as

$$\mathcal{F}_0 = \{\mathcal{F}_\beta^{(i)} \text{ for } i = 1, \dots, d_x\}, \text{ where } \beta_m \sim \begin{cases} \mathcal{N}(\beta_m^*, \sigma_0^2), & \text{if } m = 0, \\ \mathcal{N}(\beta_m^*, 0.1\sigma_0^2), & \text{if } m \in \{1, \dots, 5\}, \\ \mathcal{N}(\beta_m^*, 0.01\sigma_0^2), & \text{if } m \in \{6, \dots, 17\}, \end{cases} \quad (25)$$

where $\sigma_0^2 \in \mathbb{R}$ is the noise level of the perturbations.

Residual model \mathcal{G}_{θ_1} . We define the structure of our residual model \mathcal{G}_{θ_1} from (23) to be a convolutional neural network with learnable parameters θ_1 . We specify \mathcal{G}_{θ_1} as in Chen et al. (2022); see Chen et al. (2022) Figure 11 for details of the model correction network specification. The total number of parameters in the model \mathcal{F}_{θ_1} is 9,387, which does not depend on the state dimension d_x .

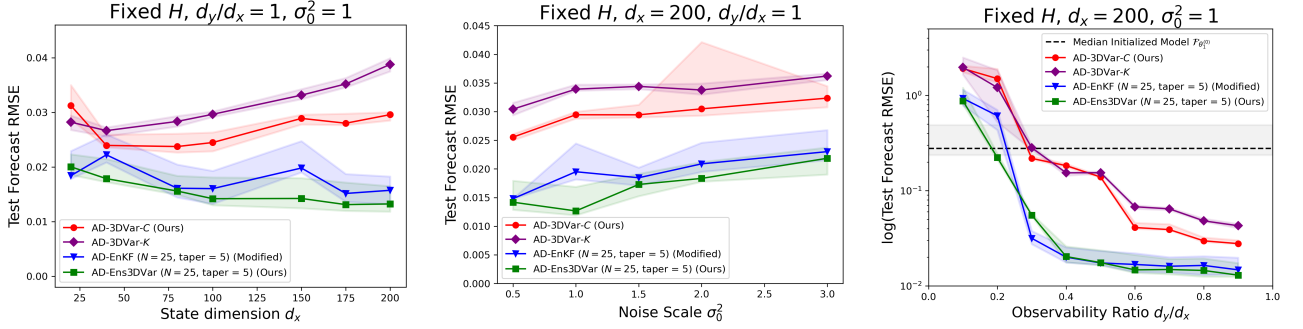
4.2.2 Results

Data generation and training details are described in Appendix F.2. We also note that in this experiment, the optimization hyperparameters used across all repeated simulations were selected from one simulation, so it is possible that closer to optimal hyperparameter sets could be chosen for each independent simulation. Across all Lorenz-96 experiments, the observation matrix H_t is held fixed across all time points t , where observed components are deterministic. For example, for every 3rd state is observed for $d_y/d_x = 0.3$. The time step used to solve the differential equation is $\Delta t = 0.05$, which corresponds to the same Δt in which observations arrive.

Performance in learning forecast parameters $\hat{\theta}_1$. Figure 4 shows the forecast performance of the learned $\mathcal{F}_{\hat{\theta}_1}$ across state dimensionalities d_x , variance of the noise σ_0^2 used to create initialized models \mathcal{F}_0 , and observability ratios d_y/d_x . The ensemble-based learning methods AD-EnKF and AD-Ens3DVar consistently outperform AD-3DVar- C and AD-3DVar- K across all experiments, as expected. AD-EnKF and AD-Ens3DVar remain robust to the state dimension d_x and noise scale σ_0^2 across various choices as seen in Figures 4a and 4b, whereas both the forecast performances of the models learned from AD-3DVar- C and AD-3DVar- K appear to increase as d_x and σ_0^2 increase. Additionally, the ensemble-based learning algorithms are able to effectively learn from sparser observational datasets than the 3DVar-based algorithms, with the ensemble-based approaches degrading when $d_y/d_x < 0.3$ while the 3DVar-based approaches start noticeably degrading in forecast performance for $d_y/d_x < 0.6$. For extremely low observability settings ($d_y/d_x = 0.1$ or $d_y/d_x = 0.2$), all methods fail to update \mathcal{F}_0 in a meaningful way, as evidenced by the forecast errors after training exceeding the forecast error of the initialized models, suggesting that the initialized models provide a better forecast model without any training. Overall, these results show that the ensemble-based AD-Ens3DVar and AD-EnKF methods are more robust than AD-3DVar- C or AD-3DVar- K to noise and can more effectively learn in low-observability regimes. However, AD-3DVar- C and AD-3DVar- K can still provide computationally cheap improvements to the forecast model in many problem settings.

Filtering performance using the learned $\hat{\theta}$ and $\hat{\phi}$. Figure 5 visualizes filtering with the learned $\hat{\theta}$ and $\hat{\phi}$ values across methods on unseen test observations with $R = I_{d_y \times d_x}$, $d_y/d_x = 0.6$, static H , $\sigma_0^2 = 1$, and $d_x = 200$ for one simulated initial imperfect model \mathcal{F}_0 . The ensemble-based methods provide the best filtering performance, with the error approximately halving compared to the 3DVar-based learning algorithms AD-3DVar- C and AD-3DVar- K . Notably, the state estimates from AD-Ens3DVar and AD-EnKF appear to have errors of consistent magnitude across observed and unobserved components of the state. On the other hand, the analyses using the learned parameters from AD-3DVar- C and AD-3DVar- K show larger errors corresponding to unobserved components, which suggests that the learned C_ϕ and K_ϕ struggle to learn the covariances corresponding

to unobserved state components, leading to increased filtering errors. This phenomenon was also observed in Figure 2 for estimating the velocity components, and is a consequence of H being held static across the entire assimilation. Additionally, an evaluation of the learned covariance inflation factor in AD-EnKF and the learned covariance mixing parameter in AD-Ens3DVar can be found in Figure 12 in Appendix F.



(a) Test forecast performance of the model \mathcal{F}_{θ_1} across state dimensionalities d_x , where $H_t = I_{d_x}$ and $\sigma_0^2 = 1$. (b) Test forecast performance of the model \mathcal{F}_{θ_1} across noise levels σ_0^2 , where $d_x = 200$ and $H_t = I_{d_x}$. (c) Test forecast performance of the model \mathcal{F}_{θ_1} across observability ratios d_y/d_x , where $d_x = 200$ and $\sigma_0^2 = 1$.

Figure 4: Lorenz-96 learned forecast performance (Section 4.2). Test performance of the learned Lorenz-96 model in (22) learned from various methods: AD-3DVar-C, AD-3DVar-K, AD-EnKF with a covariance tapering radius of 5 and $N = 25$, and AD-Ens3DVar with a covariance tapering radius of 5 and $N = 25$. The shaded regions correspond to the 0.2 and 0.8 quantiles of test forecast performances across 10 independent simulations. In the plot varying d_y/d_x , we additionally plot the median forecast RMSE for the initialized models \mathcal{F}_{β_j} for $j = 1, \dots, J = 10$ in the dashed black line (c), and the gray region corresponds to the 0.2 and 0.8 quantiles of test forecast RMSEs across these 10 initialized models.

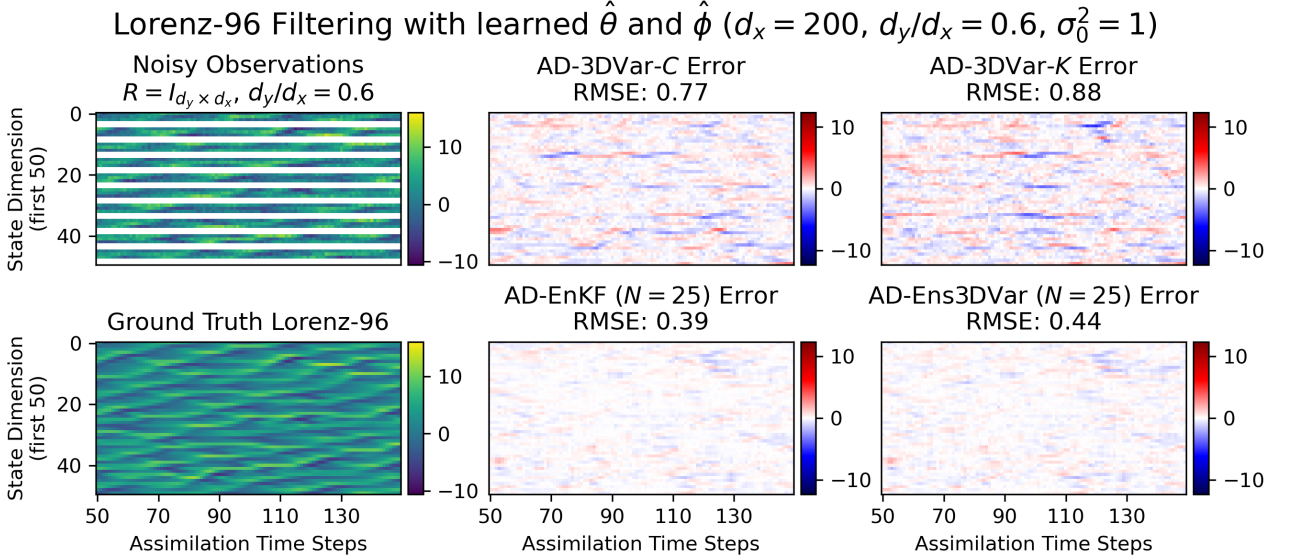


Figure 5: Lorenz-96 filtering (Section 4.2). Visualization of filtering on test observation data using the learned $\hat{\theta}$ and $\hat{\phi}$ values across the methods AD-3DVar-C, AD-3DVar-K, AD-EnKF with $N = 25$ ensemble members and a tapering radius of 5, and AD-Ens3DVar with $N = 25$ ensemble members and a tapering radius of 5 compared to the noisy observations and ground truth Lorenz-96 simulations. In this plot, the settings of the filtering problem are $R = I_{d_y \times d_x}$, $d_y/d_x = 0.6$, $\sigma_0^2 = 1$, and $d_x = 200$. For ease of visualization, only the first 50 out of 200 state components are shown in the plot. Filtering is done with the base-filtering algorithm used during training (i.e., the results presented for AD-EnKF use the learned $\hat{\theta}$ and $\hat{\phi}$ in an EnKF algorithm).

4.3 Population dynamics: Generalized Lotka-Volterra

The generalized Lotka-Volterra equations (Lotka, 1925) are

$$\frac{dx_i}{dt} = x_i f_i(x), \quad (26)$$

where $f(x) = r + Ax$, $x \in \mathbb{R}^{d_x}$ is a vector of d_x species abundances, $r \in \mathbb{R}^{d_x}$ is the species birth/death rate vector, $A \in \mathbb{R}^{d_x \times d_x}$ is the species interaction matrix, and $i = 1, \dots, d_x$ indexes the d_x total species. These equations provide a simplified model for high-dimensional species interactions in an ecosystem.

4.3.1 Learning task

In this setting, we are interested in parameter estimation. Therefore, we set $\theta_1 := \{A, r\}$, and our goal is to learn the elements of the species interaction matrix A and the birth/death rate vector r .

Hierarchical or block structures in species interactions can arise in real biological systems, and Poley et al. (2023) studies the stability of these hierarchical and block structures in generalized Lotka-Volterra equations. With this setting in mind, we learn A as a specialized block structure, where an example is given in Figure 6. Learning A consists of learning parameters $\{a_1, \dots, a_{10}\}$ that govern the block-wise interactions among the species. We specify that the number of learnable parameters is invariant to the number of species in the system, meaning the number of species contained within each block increases as d_x increases. This example is motivated by a setting where we have oracle knowledge of the group structure of species, but do not know the parameterization of the interactions among groups of species. To estimate the birth/death rate vector r , we learn a steady-state vector $x_s \in \mathbb{R}^{d_x}$ and use the property that $r = -Ax_s$ (May, 1974). Therefore, the total number of parameters estimated for \mathcal{F}_{θ_1} is $d_x + 10$.

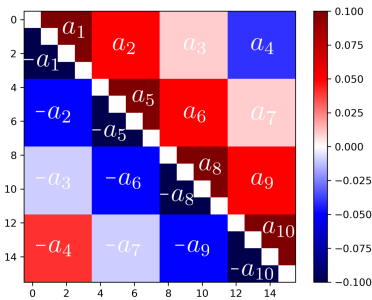


Figure 6: Example interaction matrix A for 16 interacting species in the generalized Lotka-Volterra equations. The values $\pm a_{1:10}$ denote the shared parameter values within each block.

To create imperfect initializations $\theta_1^{(0)} = \{A^{(0)}, r^{(0)}\}$, we utilize the true parameters $\theta_1^* = \{A^*, r^*\}$, where A^* is parameterized by true $a^* = \{a_1^*, \dots, a_{10}^*\}$ and r^* is constructed from the true x_s^* and the true A^* via $r^* = -A^*x_s^*$, and a noise level σ_0^2 to perturb these true values. For independent simulations $j = 1, \dots, J = 10$, we create imperfect interaction matrices via $a_j^{(0)} \sim \mathcal{N}(a^*, \sigma_0^2 I_{10 \times 10})$, and similarly construct $x_j^{(0)} \sim \mathcal{N}(x_s^*, \sigma_0^2 I_{d_x \times d_x})$ and solve $r_j^{(0)} = -A_j^{(0)}x_j^{(0)}$.

4.3.2 Results

We focus on a setting common to many problems in systems biology: one where the system is only partially observed at any given time, and the components (species) observed (and the number of observed components) may change across time. Therefore, H_t varies with time and $d_{y_t}/d_x < 1$. In our experiments, for each time point t , the observed species are randomly selected such that the ratio d_{y_t}/d_x is fixed across time. We investigate the performance of AD-3DVar-C, AD-EnKF, and AD-Ens3DVar, which are able to handle time-varying H_t . We omit AD-3DVar-K, since this method is *not* able to handle observational data of this form. Training and data generation details are outlined in Appendix F. Optimization hyperparameters were tuned for each simulation and parameter value across the $J = 10$ independent simulated initial models. The time step used to solve the differential equation is $\Delta t = 0.05$, which corresponds to the same Δt in which observations arrive.

Performance in learning forecast parameters $\hat{\theta}_1$. Figure 7 visualizes the performance across the methods AD-3DVar-C, AD-EnKF, and AD-Ens3DVar in recovering the ground truth parameters $\theta_1^* := \{A^*, r^*\}$ for a variety of settings, where the number of species d_x in the system, the proportion of species that are observed d_{y_t}/d_x , and the training dataset size T are all varied. Across all results in Figure 7, AD-EnKF and AD-Ens3DVar perform similarly, with AD-EnKF performing better with some parameter choices. The performance of both ensemble-based methods remain relatively robust to the choices of parameters considered. AD-3DVar-C exhibits a bit more volatile behavior across parameter values, particular for varied species d_x and training size T , which could be in part due to suboptimal hyperparameter selections from observational validation data.

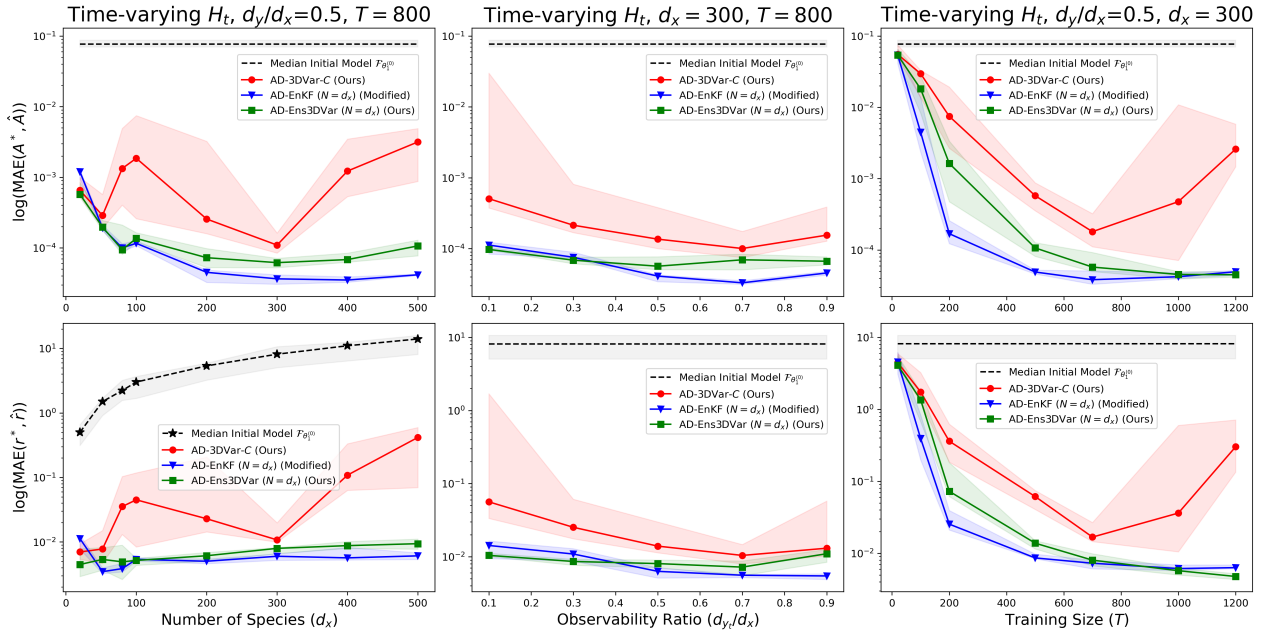


Figure 7: Generalized Lotka-Volterra parameter estimation (Section 4.3). Parameter estimation mean absolute errors (MAEs) of the learned generalized Lotka-Volterra model in (26) learned from the methods AD-3DVar-C, AD-EnKF with $N = d_x$, and AD-Ens3DVar with $N = d_x$. The shaded regions correspond to the 0.2 and 0.8 quantiles of test forecast performances across 10 independent simulations. In each plot, we plot the median MAEs for the initialized models $\mathcal{F}_{\theta_j^0}$ for $j = 1, \dots, J = 10$ in the dashed black line, and the gray region corresponds to the 0.2 and 0.8 quantiles of test forecast RMSEs across these 10 initialized models. The top row of plots correspond to the error in the estimated interaction matrix \hat{A} component of $\hat{\theta}_1$, and the second row of plots correspond to the error in the estimated population change vector \hat{r} component of $\hat{\theta}_1$.

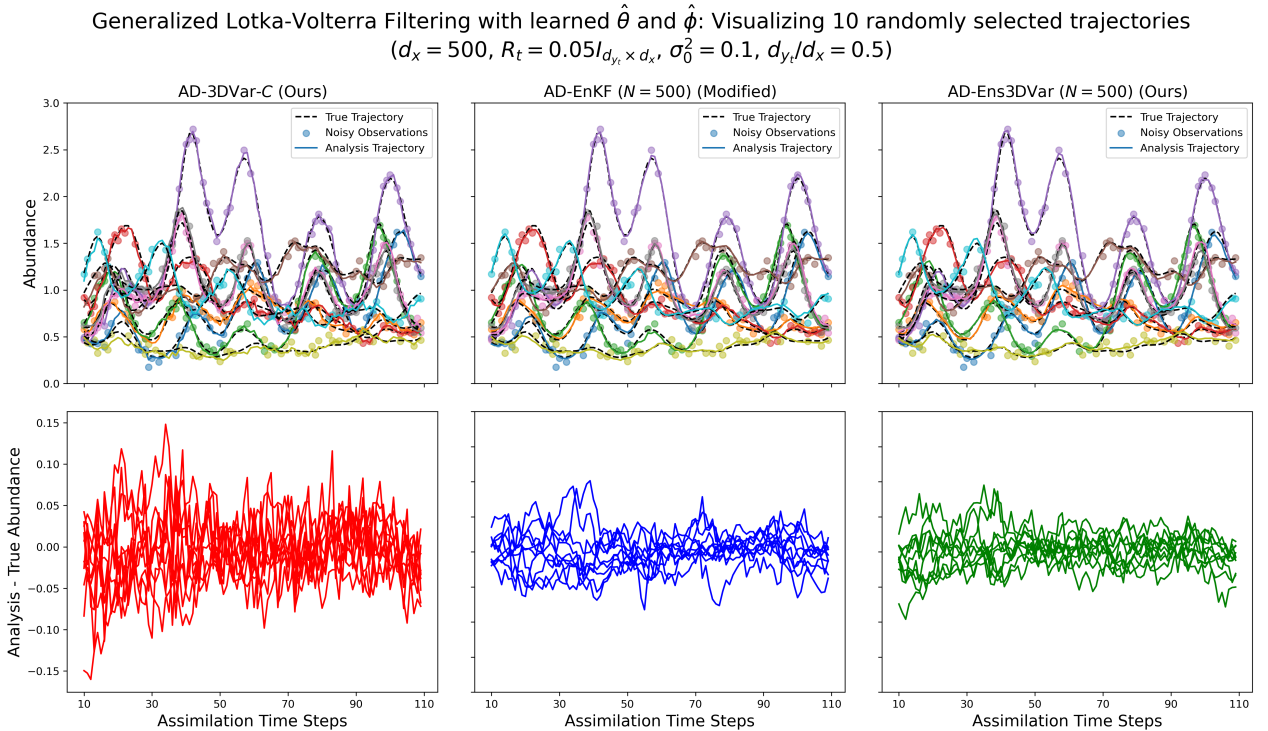


Figure 8: Generalized Lotka-Volterra filtering (Section 4.3). Visualization of filtering on test observational data using the learned $\hat{\theta}$ and $\hat{\phi}$ values across the methods AD-3DVar-C, AD-EnKF with $N = 500$ ensemble members, and AD-Ens3DVar with $N = 500$ ensemble members where $d_x = 500$, $R_t = 0.05I_{d_{y_t} \times d_x}$, $\sigma_0^2 = 0.1$, and $d_{y_t}/d_x = 0.5$. For ease of visualization, only 10 randomly selected species abundance trajectories out of the 500 total species are visualized. In each plot in the first row, the true trajectories are given by the dashed black lines, the sparse, noisy observation are plotted as a scatterplot, and the analyses are plotted as solid colored lines. The second row plots the errors in the analyses compared to the ground truth trajectories.

Filtering performance using the learned $\hat{\theta}$ and $\hat{\phi}$. Figure 8 visualizes the analyses when filtering with the learned $\hat{\theta}$ and $\hat{\phi}$ parameters from the methods AD-3DVar-*C*, AD-EnKF, and AD-Ens3DVar for the parameter settings $d_x = 500$, $R_t = 0.05I_{d_{y_t} \times d_x}$, $\sigma_0^2 = 0.1$, and $d_{y_t}/d_x = 0.5$. This figure shows that all three methods are able to recover reasonable estimates of the species abundance trajectories given sparse, noisy observations where H_t varies over time. As is consistent with our results in Figure 7, the ensemble-based methods AD-EnKF and AD-Ens3DVar provide better estimates of the ground truth abundance trajectories, and AD-3DVar exhibits larger errors in the analyses. All methods, however, produce reasonable reconstructions of the species trajectories. An evaluation of the learned covariance inflation factor in AD-EnKF and the learned covariance mixing parameter in AD-Ens3DVar for the generalized Lotka-Volterra system can be found in Figure 12 in Appendix F.

5 Discussion

This work proposes a general framework for jointly learning states, forecasting parameters, and filtering parameters via noisy and potentially sparse observations of dynamical systems. Our approach achieves this goal by leveraging filtering algorithms in an offline learning optimization algorithm. We outline and compare particular special cases of our framework that may be used directly by practitioners; however, we note that similar learning algorithms from our general framework. As previously emphasized, there is no one formulation of our auto-differentiable filtering framework that is best suited for all problems, which leads practitioners to make informed choices for their particular application. We now provide general guidelines for practitioners to consider when making these choices for their particular application, informed by our results. In addition, we discuss possible future directions that stem from this work.

5.1 General guidelines for practitioners

The following discussion of the general guidelines for practitioners when selecting or constructing an auto-differentiable filtering algorithm is summarized in Table 3.

We first discuss when it is advantageous to learn θ and ϕ with the ensemble-based learning approaches, AD-Ens3DVar or AD-EnKF. Across all experiments, the ensemble-based filtering approaches provided the best performance in forecasting with the learned forecast model and in filtering with the learned forecast and filter components. However, this performance comes at the price of higher computational cost and memory footprint. Therefore, if accuracy is of utmost importance to a practitioner, AD-EnKF or AD-Ens3DVar would be the preferred choices. Another setting where AD-EnKF or AD-Ens3DVar would be preferred is when the observation matrix $H_t \equiv H$ is fixed. As noted in Sections 4.1 and 4.2, when some state components are completely unobserved for the entire time series trajectory, the lighter-weight methods AD-3DVar-*C* and AD-3DVar-*K* struggle to accurately estimate these components on test data, whereas this phenomenon did not occur with the ensemble-based learning methods. One significant consideration with ensemble-based methods, however, is their memory footprint, which may be prohibitive for off-the-shelf use in high-dimensional settings and may require simplifying modifications to be used.

For settings where computational speed is important, particularly in high-dimensional settings, AD-3DVar-*C* or AD-3DVar-*K* could be preferable since these approaches are computationally cheaper and memory-light. AD-3DVar-*C* could be particularly useful in settings where H_t is time-varying, since this method can learn reasonable approximations of all state components, as seen in Figure 8. AD-3DVar-*C* can compute off-the-shelf on higher-dimensional problems compared to ensemble-based methods without simplifying modifications. Since AD-3DVar-*K* is even lighter-weight than AD-3DVar-*C*, if a practitioner is especially in need of a fast computational learning method, AD-3DVar-*K* could be useful in settings where H is fixed for the entire time series. However, this method may come with a slight degradation in the ability to improve a forecast model and filter with the learned Kalman gain.

5.2 Future directions

For high-dimensional systems, AD-Ens3DVar and AD-EnKF may be computationally or memory prohibitive off-the-shelf; therefore, one may consider making simplifying modifications to break the problem down into smaller, parallelizable tasks. For example, a modified version of EnKF that allows for parallelization, particularly the local ensemble transform Kalman filter (LETKF) (Ott et al., 2004; Hunt et al., 2007) algorithm may provide comparable accuracy while allowing for computation on large-scale problems using multiple GPUs for high-dimensional systems where large ensembles are needed. These modifications can be made for practitioners desiring a learning method that is both scalable to high-dimensional problems and accurate. Evaluating an AD-LETKF type of algorithm is left as a future direction.

Algorithm	$H_t \equiv H$	Time-varied H_t	High-dimensional d_x	Memory	Learning \mathcal{F}_{θ_1}
AD-EnKF (Modified) (Chen et al., 2022)	Reasonably recovers all states	✓	May require non-trivial modifications	High; scales with N	Accurate
AD-Ens3DVar (Ours)	Reasonably recovers all states	✓	May require modifications or small N	High; scales with N	Accurate
AD-3DVar- C (Ours)	Struggles to recover unobserved states	✓	Computation scales better for large d_x	Lower	Moderate accuracy
AD-3DVar- K (Levine and Stuart, 2022)	Struggles to recover unobserved states	✗	Computation scales best for large d_x	Lowest	Moderate accuracy

Table 3: Summary table of particular examples of auto-filtering algorithms in terms of their ability to learn accurate filtering parameters when $H_t \equiv H$ when $d_y < d_x$, ability to filter with a time-varying H_t , relative scalability to high-dimensional systems, relative memory footprint, and relative accuracy in improving the forecast model \mathcal{F}_{θ_1} .

As previously noted, the formulation of our optimization task is offline, and all of our experiments operate in this setting. However, one can easily imagine slight modifications that allow for on-the-fly corrections to the forecast and filtering parameters through an online learning approach. This modification would be particularly of interest in settings where near-real-time inference is required. Moreover, it is known that smoothing-based data assimilation methods provide more accurate state estimation, and therefore may provide more accurate learning of forecast and filtering parameters. Though more computationally costly, an interesting future direction would be to assess the computational feasibility and empirical gain from a similar learning framework that utilizes smoothing rather than filtering. The framework presented in this work lays the foundation for further development in these directions.

Acknowledgments

This research was supported in part by grants from the NSF (DMS-2235451) and Simons Foundation (MPS-NITMB-00005320) to the NSF-Simons National Institute for Theory and Mathematics in Biology (NITMB). We also gratefully acknowledge the support of DOE OJ-60040-0023A and AFOSR FA9550-24-1-0327. The work of DSA was partly funded by the NSF CAREER award DMS-2237628. MA was partly supported by the NSF Graduate Research Fellowship Program under Grant No. DGE-1746045.

References

- Adrian, M., Sanz-Alonso, D., and Willett, R. (2025). Data assimilation with machine learning surrogate models: A case study with FourCastNet. *Artificial Intelligence for the Earth Systems*, 4(3):e240050.
- Aicher, C., Foti, N. J., and Fox, E. B. (2020). Adaptively truncating backpropagation through time to control gradient bias. *Proceedings of The 35th Uncertainty in Artificial Intelligence Conference*, 115:799–808.
- Al-Ghathas, O. and Sanz-Alonso, D. (2024). Non-asymptotic analysis of ensemble Kalman updates: effective dimension and localization. *Information and Inference: A Journal of the IMA*, 13(1):iaad043.
- Anderson, J. L. (2012). Localization and sampling error correction in ensemble Kalman filter data assimilation. *Monthly Weather Review*, 140(7):2359–2371.
- Bach, E., Baptista, R., Calvello, E., Chen, B., and Stuart, A. (2026). Learning enhanced ensemble filters. *Journal of Computational Physics*, 547:114550.
- Bach, E., Baptista, R., Luk, E., and Stuart, A. (2025a). Learning optimal filters using variational inference. <https://arxiv.org/abs/2406.18066>.
- Bach, E., Baptista, R., Sanz-Alonso, D., and Stuart, A. (2025b). Machine learning for inverse problems and data assimilation. <https://arxiv.org/abs/2410.10523>.

- Baydin, A. G., Pearlmutter, B. A., Radul, A. A., and Siskind, J. M. (2018). Automatic differentiation in machine learning: a survey. *Journal of Machine Learning Research*, 18(153):1–43.
- Bocquet, M., Farchi, A., and Malartic, Q. (2021). Online learning of both state and dynamics using ensemble Kalman filters. *Foundations of Data Science*, 3(3):305–330.
- Brajard, J., Carrassi, A., Bocquet, M., and Bertino, L. (2020). Combining data assimilation and machine learning to emulate a dynamical model from sparse and noisy observations: A case study with the Lorenz 96 model. *Journal of Computational Science*, 44:101171.
- Brunton, S. L., Proctor, J. L., and Kutz, J. N. (2016). Discovering governing equations from data by sparse identification of nonlinear dynamical systems. *Proceedings of the National Academy of Sciences*, 113(15):3932–3937.
- Chakraborty, D., Guan, H., Stock, J., Arcomano, T., Cervone, G., and Maulik, R. (2025). Multimodal atmospheric super-resolution with deep generative models. *Machine Learning: Earth*, 2(1):015001.
- Chen, N. (2023). *Stochastic Methods for Modeling and Predicting Complex Dynamical Systems*. Springer.
- Chen, X. and Li, Y. (2025). An overview of differentiable particle filters for data-adaptive sequential Bayesian inference. *Foundations of Data Science*, 7(4):915–943.
- Chen, Y., Sanz-Alonso, D., and Willett, R. (2022). Autodifferentiable ensemble Kalman filters. *SIAM Journal on Mathematics of Data Science*, 4(2):801–833.
- Chen, Y., Sanz-Alonso, D., and Willett, R. (2023). Reduced-order autodifferentiable ensemble Kalman filters. *Inverse Problems*, 39(12):124001.
- Chinellato, E. and Marcuzzi, F. (2025). State, parameters and hidden dynamics estimation with the deep Kalman filter: Regularization strategies. *Journal of Computational Science*, 87:102569.
- Clohessy, W. H. and Wiltshire, R. S. (1960). Terminal guidance system for satellite rendezvous. *Journal of the Aerospace Sciences*, 27(9):653–658.
- Courtier, P., Thépaut, J.-N., and Hollingsworth, A. (1994). A strategy for operational implementation of 4D-Var, using an incremental approach. *Quarterly Journal of the Royal Meteorological Society*, 120(519):1367–1387.
- Evensen, G. (1994). Sequential data assimilation with a nonlinear quasi-geostrophic model using Monte Carlo methods to forecast error statistics. *Journal of Geophysical Research: Oceans*, 99(C5):10143–10162.
- Evensen, G. (2003). The ensemble Kalman filter: Theoretical formulation and practical implementation. *Ocean Dynamics*, 53(4):343–367.
- Farchi, A., Laloyaux, P., Bonavita, M., and Bocquet, M. (2021). Using machine learning to correct model error in data assimilation and forecast applications. *Quarterly Journal of the Royal Meteorological Society*, 147(739):3067–3084.
- Furrer, R. and Bengtsson, T. (2007). Estimation of high-dimensional prior and posterior covariance matrices in Kalman filter variants. *Journal of Multivariate Analysis*, 98(2):227–255.
- Gandin, L. S. (1966). Objective analysis of meteorological fields. Translated from the Russian. Jerusalem (Israel Program for Scientific Translations). *Quarterly Journal of the Royal Meteorological Society*, 92(393):447–447.
- Gaspari, G. and Cohn, S. E. (1999). Construction of correlation functions in two and three dimensions. *Quarterly Journal of the Royal Meteorological Society*, 125(554):723–757.
- Gottwald, G. A. and Reich, S. (2021). Combining machine learning and data assimilation to forecast dynamical systems from noisy partial observations. *Chaos: An Interdisciplinary Journal of Nonlinear Science*, 31(10):101103.
- Griewank, A. and Walther, A. (2008). *Evaluating Derivatives*. Society for Industrial and Applied Mathematics, second edition.
- Hamill, T. M. and Snyder, C. (2000). A hybrid ensemble Kalman filter–3D variational analysis scheme. *Monthly Weather Review*, 128(8):2905 – 2919.
- Hill, G. W. (1878). Researches in the lunar theory. *American Journal of Mathematics*, 1(1):5–26.

- Houtekamer, P. L. and Mitchell, H. L. (1998). Data assimilation using an ensemble Kalman filter technique. *Monthly Weather Review*, 126(3):796 – 811.
- Hunt, B. R., Kostelich, E. J., and Szunyogh, I. (2007). Efficient data assimilation for spatiotemporal chaos: A local ensemble transform Kalman filter. *Physica D: Nonlinear Phenomena*, 230(1):112–126. Data Assimilation.
- Kalman, R. E. (1960). A new approach to linear filtering and prediction problems. *Journal of Basic Engineering*, 82(1):35–45.
- Levine, M. E. and Stuart, A. M. (2022). A framework for machine learning of model error in dynamical systems. *Communications of the American Mathematical Society*, 2(07):283–344.
- Liu, C., Xiao, Q., and Wang, B. (2008). An ensemble-based four-dimensional variational data assimilation scheme. Part I: Technical formulation and preliminary test. *Monthly Weather Review*, 136(9):3363 – 3373.
- Lorenc, A. C. (1986). Analysis methods for numerical weather prediction. *Quarterly Journal of the Royal Meteorological Society*, 112(474):1177–1194.
- Lorenz, E. (1995). *Predictability: a problem partly solved*. PhD thesis, Shinfield Park, Reading.
- Lotka, A. J. (1925). *Elements of Physical Biology*. Williams and Wilkins Company, Baltimore, Maryland.
- Lu, F. (2025). U-Net Kalman filter (UNetKF): An example of machine learning-assisted data assimilation. *Journal of Advances in Modeling Earth Systems*, 17(4).
- Lunderman, S., Morzfeld, M., and Posselt, D. J. (2021). Using global Bayesian optimization in ensemble data assimilation: parameter estimation, tuning localization and inflation, or all of the above. *Tellus A: Dynamic Meteorology and Oceanography*, 73(1):1–16.
- Mandel, J. (2006). Efficient implementation of the ensemble Kalman filter. Technical Report 231, Center for Computational Mathematics, University of Colorado at Denver and Health Sciences Center, Denver, CO.
- May, R. M. (1974). *Stability and Complexity in Model Ecosystems*, volume 1. Princeton University Press.
- Melinc, B. and Zaplotnik, Z. (2024). 3D-Var data assimilation using a variational autoencoder. *Quarterly Journal of the Royal Meteorological Society*, 150(761):2273–2295.
- Ott, E., Hunt, B. R., Szunyogh, I., Zimin, A. V., Kostelich, E. J., Corazza, M., Kalnay, E., Patil, D., and Yorke, J. A. (2004). A local ensemble Kalman filter for atmospheric data assimilation. *Tellus A: Dynamic Meteorology and Oceanography*, 56(5):415–428.
- Palmer, T. N., Molteni, F., Mureau, R., Buizza, R., Chapelet, P., and Tribbia, J. (1992). Ensemble prediction. ECMWF Research Department Technical Memorandum 188, European Centre for Medium-Range Weather Forecasts.
- Parrish, D. F. and Derber, J. C. (1992). The National Meteorological Center’s spectral statistical-interpolation analysis system. *Monthly Weather Review*, 120(8):1747 – 1763.
- Poley, L., Baron, J. W., and Galla, T. (2023). Generalized Lotka-Volterra model with hierarchical interactions. *Phys. Rev. E*, 107:024313.
- Revach, G., Shlezinger, N., Ni, X., Escoriza, A. L., van Sloun, R. J. G., and Eldar, Y. C. (2022). KalmanNet: Neural network aided Kalman filtering for partially known dynamics. *IEEE Transactions on Signal Processing*, 70:1532–1547.
- Richardson, L. F. (1922). *Weather Prediction by Numerical Process*. Cambridge University Press.
- Sanderse, B., Stinis, P., Maulik, R., and Ahmed, S. E. (2025). Scientific machine learning for closure models in multiscale problems: A review. *Foundations of Data Science*, 7(1):298–337.
- Sanz-Alonso, D. and Waniorek, N. (2025). Long-time accuracy of ensemble Kalman filters for chaotic dynamical systems and machine-learned dynamical systems. *SIAM Journal on Applied Dynamical Systems*, 24(3):2246–2286.
- Sutskever, I., Vinyals, O., and Le, Q. V. (2014). Sequence to sequence learning with neural networks. <https://arxiv.org/abs/1409.3215>.
- Tippett, M. K., Anderson, J. L., Bishop, C. H., Hamill, T. M., and Whitaker, J. S. (2003). Ensemble square root filters. *Monthly Weather Review*, 131(7):1485–1490.

- Wang, Z. and Jiang, L. (2025). Reinforcement learning based data assimilation for unknown state model.
<https://arxiv.org/abs/2511.02286>.
- Ścibior, A. and Wood, F. (2021). Differentiable particle filtering without modifying the forward pass.
<https://arxiv.org/abs/2106.10314>.

A Specification of C_ϕ in AD-3DVar-C

As discussed in the main text, we specify in AD-3DVar-C that we learn B_ϕ such that $C_\phi = B_\phi B_\phi^\top$, where we learn elements of the dense matrix $B_\phi \in \mathbb{R}^{d_x \times d_x}$. In practice, particularly for large-scale systems, it may be infeasible to learn a dense matrix $B_\phi \in \mathbb{R}^{d_x \times d_x}$ since this matrix may be too large to store, or even if it is small enough to store, learning this dense matrix may introduce additional computation that may be avoided by learning a more efficient choice of B_ϕ . One alternative option is to learn a sparse upper triangular matrix B_ϕ^U such that $C_\phi = B_\phi^U (B_\phi^U)^\top$ with $|\phi| \leq \frac{1}{2}d_x(d_x + 1)$, where sparsity constraints on the upper diagonal structure of B_ϕ^U reduce the number of learnable parameters and reduce memory by only storing nonzero elements.

Another alternative that we more thoroughly explore is defining C_ϕ such that we learn a low-rank update to some initial C_0 . Specifically, we consider parameterizations of the form

$$C_\phi = C_0 + B_\phi B_\phi^\top, \quad (27)$$

where $B_\phi \in \mathbb{R}^{d_x \times p}$ and $p \ll d_x$. This setting assumes that we have some reasonable initialization of C_ϕ , potentially constructed based on domain knowledge and the performance of the initialized $\mathcal{F}_{\theta_1^{(0)}}$, which we want to efficiently improve with a low-rank update.

We numerically investigate the performance of AD-3DVar-C with low-rank parameterization of C_ϕ using the Lorenz-96 system under different observability ratios. Details on the training task on Lorenz-96 data can be found in Section F. We explore the impact of the choice of p (the maximum rank of B_ϕ) on our ability to learn an improved forecast model \mathcal{F}_{θ_1} , and these results are visualized in Figure 9. In this experiment, $p \in [50, 75, 100, 150, 175, 200]$, $d_x = 200$, $d_y/d_x \in [0.3, 0.5, 0.8]$, $\sigma_0^2 = 1$, H_t varies with time t with randomly selected observed dimensions at each time point, and $C_0 = I_{d_x}$. Figure 9 shows that learning a low rank update for high observability regimes (e.g., $d_y/d_x = 0.8$) remains robust across choices of p up until approximately $p = d_x/2$. This robustness degrades as the observability decreases. This experiment shows evidence that learning a low-rank update can be feasible, but the performance of the learned model can vary depending on specific aspects of the problem, including how low-rank B_ϕ is specified to be.

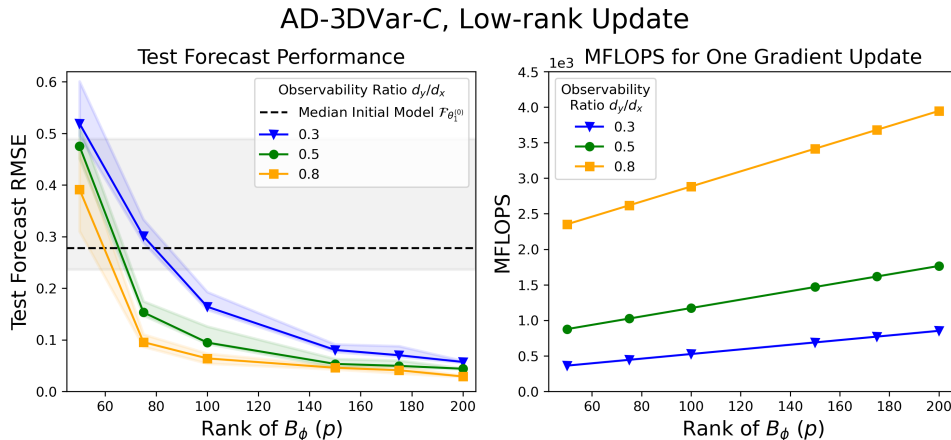


Figure 9: Experiment based on the Lorenz-96 system described in Section 4.2. **(Left)** Median test forecast RMSE for learning a low rank update to the background covariance such that $C_\phi = C_0 + B_\phi B_\phi^\top$, where $B_\phi \in \mathbb{R}^{d_x \times p}$ and $p < d_x$. In this experiment, $d_x = 200$, $d_y/d_x \in [0.3, 0.5, 0.8]$, $\sigma_0^2 = 1$, and observations at each time t are randomly sampled across state dimensions (i.e., H_t varies with time). Each training task was replicated for $J = 10$ independent simulations. We additionally plot the median forecast RMSE for the initialized models $\mathcal{F}_{\beta^{(j)}}$ for $j = 1, \dots, M$ in the dashed black line, and the gray region corresponds to the 0.2 and 0.8 quantiles of test forecast RMSEs across these 10 initialized models. **(Right)** Plot of millions of floating point operations per second (MFLOPS) across values of p for processing one subsequence (both the forward and backward pass) for the setting where $d_x = 200$, $p \in [50, 75, 100, 150, 175, 200]$, $L = 20$, and $d_y/d_x \in [0.3, 0.5, 0.8]$.

B Auto-differentiable filtering with TBPTT

For all experiments, we implement a modification of Algorithm 1 that includes truncated backpropagation through time (TBPTT), which aids in preventing vanishing or exploding gradients. TBPTT also aids in memory management since the computational graph only needs to be stored for a time series of length L instead of the entire length T time series, where $L \ll T$. This modified algorithm is shown in Algorithm 2 and includes the

additional parameter L , which controls how often the parameters θ and ϕ are updated per epoch while training on the entire length T time series.

Algorithm 2 Auto-differentiable filtering with TBPTT

Input: Initial time samples $x_0^{1:N}$ with ensemble size N , observations $y_{1:T}$, initialized forecast model $\mathcal{M}_{\theta^{(0)}}(\cdot)$, initialized Kalman gain $\mathcal{K}_{\phi^{(0)}}(\cdot)$, observation perturbation model $\mathcal{Y}(\cdot; R_{1:T})$, observation matrices $H_{1:T}$, number of time points to assimilate before backpropagation L

while θ, ϕ are not converging: **do**

for $j = 0, \dots, T/L - 1$ **do**

$t_0 = jL; t_1 = \min\{(j+1)L, T\}$

$x_{t_0:t_1}^{1:N, (k)} = \text{Filter}(x_{t_0}^{1:N}, y_{t_0:t_1}; \mathcal{M}_{\theta^{(k)}}(\cdot), \mathcal{K}_{\phi^{(k)}}(\cdot), \mathcal{Y}(\cdot; R_{t_0:t_1}), H_{t_0:t_1})$

\triangleright Eq. (4)

$\mathcal{L}(\theta^{(k)}, \phi^{(k)}) = -\sum_{t=t_0}^{t_1} \log \mathcal{N}(y_t; H_t \hat{m}_t^{\theta^{(k)}}, H_t C_t^{\theta^{(k)}, \phi^{(k)}} H_t^\top + R_t)$

$\theta^{(k+1)} = \theta^{(k)} - \alpha_{1,k} \nabla_{\theta} \mathcal{L}(\theta^{(k)}, \phi^{(k)})$

$\phi^{(k+1)} = \phi^{(k)} - \alpha_{2,k} \nabla_{\phi} \mathcal{L}(\theta^{(k)}, \phi^{(k)})$

$k \leftarrow k + 1$

end for

end while

Output: Analysis estimates $x_{1:T}^{1:N}$, learned forecast parameters $\hat{\theta}$, learned analysis parameters $\hat{\phi}$

C Learning the covariance tapering matrix ρ as part of ϕ in AD-EnKF (Modified)

We can modify (8) to include learning of the covariance tapering matrix by rewriting the equation as

$$\hat{C}_t^{\theta, \phi} = (1 + \phi_1)(\rho(\phi_2) \circ \hat{C}_t^{\theta}), \quad (28)$$

where ϕ_1 corresponds to the covariance inflation factor, $\rho(\phi_2)$ is a tapering matrix with tapering radius ϕ_2 , and $\phi = \{\phi_1, \phi_2\}$. A common way to specify the tapering matrix, particularly in applications with spatial components, is via the Gaspari-Cohn tapering function (Gaspari and Cohn, 1999). We adopt this standard parameterization of the tapering matrix in what follows.

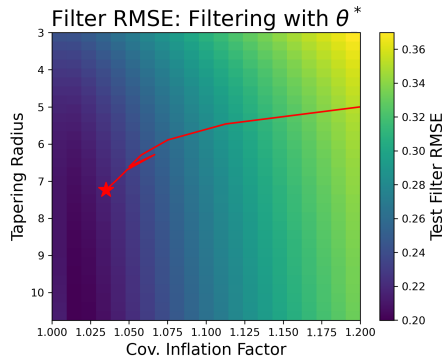


Figure 10: Heatmap of the EnKF filter RMSE values when filtering with the true \mathcal{F}_{θ^*} on unseen test data across different choices of tapering radius and covariance inflation for $d_x = 40$, $d_y/d_x = 1$, and $\sigma_0^2 = 1$. The red trajectory corresponds to the convergence of the analysis parameter vector $\phi \in \mathbb{R}^2$ for the covariance tapering and inflation for AD-EnKF (Modified), which was initialized at tapering = 5 and inflation = 1.2. The red star corresponds to location of the converged value for the (tapering, inflation) pair.

Figure 5 shows the convergence of the $\phi \in \mathbb{R}^2$ parameters for AD-EnKF (Modified) that learn the covariance inflation and the tapering radius superimposed on the test filter RMSE of EnKF with the true θ^* parameters. We can see that the optimization trajectory correctly traverses to an area of low test filter RMSE, but does not necessarily attain the minimum test filter loss. This result is due to the fact that observation noise impacts the optimization landscape, which can lead to convergence to a suboptimal region.

We also note that learning the covariance tapering radius *can be extremely computationally expensive, even for small d_x* due to the fact that $\rho(\phi_2)$ needs to be recomputed every time ϕ_2 is updated after backpropagation. When implementing TBPTT as discussed in Appendix B, parameters are updated $\lceil T/L \rceil$ times per epoch. Since this matrix can be large with many elements, frequently updating this matrix and backpropagating through

can be computationally expensive. As an alternative to gradient-based learning, one could choose a best initial guess of $\phi_2^{(0)}$, fix it during AD-EnKF (Modified) training, then perform a grid search over possible choices of ϕ_2 by evaluating EnKF with $\hat{\phi}$ and $\hat{\theta}$ based on the forecast log-likelihood on validation observations (i.e., Eq. (14) with held-out validation observations). This process is likely to be computationally lighter than a gradient-based learning approach.

D Varying the ensemble size N for AD-EnKF (Modified) and AD-Ens3DVar

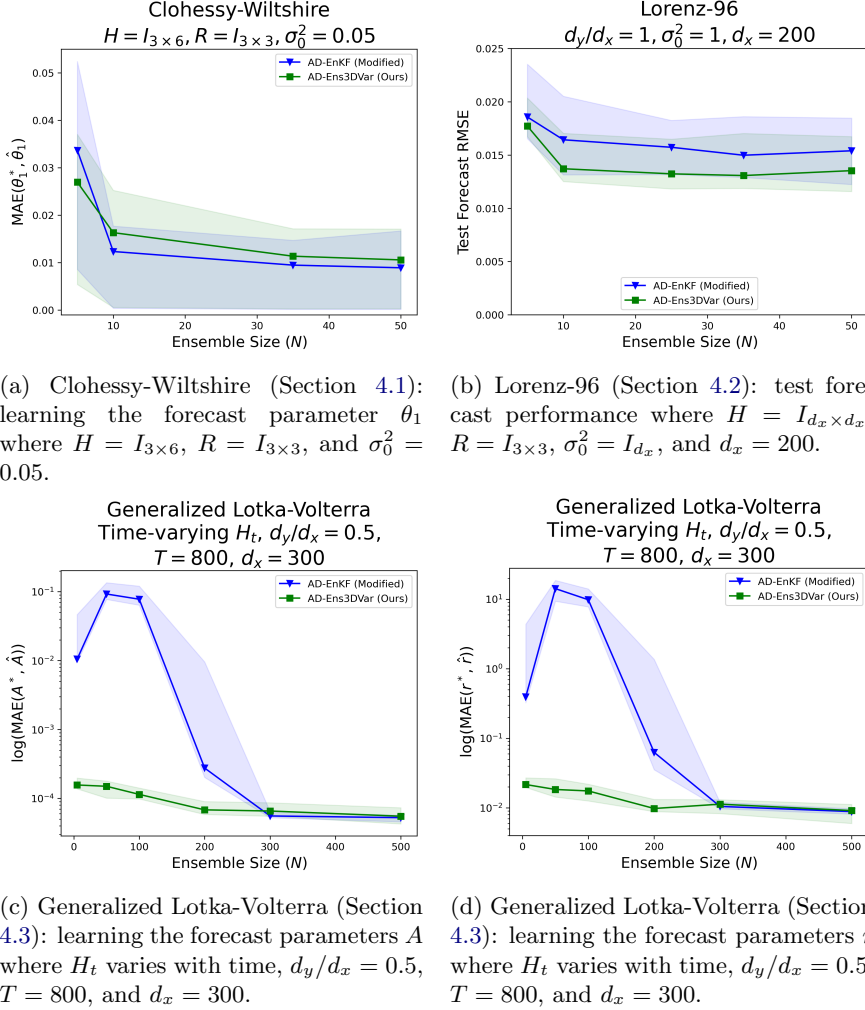


Figure 11: Varying the ensemble size for AD-EnKF (Modified) and AD-Ens3DVar for the Clohessy-Wiltshire (Section 4.1), Lorenz-96 (Section 4.2), and generalized Lotka-Volterra (Section 4.3) examples. The shaded regions correspond to the 0.2 and 0.8 quantiles of forecast performance or forecast parameter estimation error across 10 independent simulations.

Figure 11 shows the evaluation of the learned forecast models across independent simulations for varying ensemble sizes used in AD-EnKF (Modified) and AD-Ens3DVar. Figures 11a, 11c, and 11d show a sharp degradation in the ability of AD-EnKF (Modified) to learn the true forecast model parameters θ_1^* when $N < d_x$. This performance degradation can be attributed to the fact that covariance tapering was not used in the Clohessy-Wiltshire or generalized Lotka-Volterra examples, which leads to poor state estimation from EnKF, and therefore a limited ability to learn from this estimation. This phenomenon is less apparent in the Lorenz-96 example in Figure 11b since a covariance tapering radius of 5 is used, and therefore better state estimation for EnKF is possible for $N < d_x$.

AD-Ens3DVar does not suffer from this degradation in performance due to the additional learned time-independent 3DVar-type covariance matrix that is mixed with an EnKF-type covariance via a learnable covariance mixing weight. Since the covariance mixing parameter is learned, AD-Ens3DVar has the ability to automatically shift the mixing parameter away from the poorly estimated EnKF covariance matrix in favor of

the more stable 3DVar-type covariance. Therefore, AD-Ens3DVar provides a more flexible means to learn from observations that better combats ensemble-based failure modes.

For $N > d_x$, AD-Ens3DVar and AD-EnKF (Modified) perform comparably, with no clear advantage in performance for one method versus the other at fixed ensemble sizes.

E Evaluation metrics

Forecast RMSE. We compute the test forecast root mean square error (RMSE) in the Lorenz-96 experiments to evaluate the performance of the learned model $\mathcal{F}_{\hat{\theta}_1}$ against the true model $\mathcal{F}_{\theta_1^*}$. To compute these forecast errors, we randomly select $P = 500$ states on the Lorenz-96 attractor to serve as initial conditions for forecasts, and compute one-step-ahead forecasts using the true and learned dynamics. The forecast-RMSE is computed as follows

$$\text{forecast-RMSE} = \sqrt{\frac{1}{d_x P} \sum_{p=1}^P \|\mathcal{F}_{\hat{\theta}_1}(x_p) - \mathcal{F}_{\theta_1^*}(x_p)\|^2}, \quad (29)$$

where x_p for $p = 1, \dots, P$ is an initial condition sampled on the Lorenz-96 attractor, and a one-step-ahead forecast is computed for each of these P initial conditions with the imperfect $\mathcal{F}_{\hat{\theta}_1}$ and the true dynamics \mathcal{F} .

Filter RMSE. Filter RMSE is computed as

$$\text{filter-RMSE} = \sqrt{\frac{1}{d_x T} \sum_{t=1}^T \|x_t - x_t^*\|^2}, \quad (30)$$

where $x_t = \frac{1}{N} \sum_{n=1}^N x_t^n$ is the analysis mean at time t computed with N ensemble members, and x_t^* is the ground truth state at time t .

Parameter Estimation MAE. We compute the parameter estimation mean absolute error (MAE) in our generalized Lotka-Volterra and Clohessy-Wiltshire examples as

$$\text{MAE} = \frac{1}{|\theta_1^*|} \|\hat{\theta}_1 - \theta_1^*\|_1, \quad (31)$$

where $|\theta_1^*|$ is the number of parameters in vector of true forecast model parameters θ_1^* , and $\hat{\theta}_1$ is the vector of estimated forecast model parameters.

F Supplementary experimental details

General training details. In all experiments, forecast error metrics are computed based on the average forecast errors in the last 10 epochs, with 40 epochs of training total. All experiments demonstrate proper convergence well before training for the full 40 epochs. We additionally utilize the `torch.optim.Adam` optimizer with varied learning rates for θ and ϕ depending on the experiment, with the remaining settings set to default. We use the `torch.optim.lr_scheduler.ReduceLROnPlateau` scheduler, where the patience is set to 5 epochs with the remaining settings set to default. For hyperparameter tuning the learning rates for θ and ϕ , we tuned these hyperparameters based on the forecast log-likelihood evaluated at validation observations for 4 independent validation trajectories. All experiments are computed using a single GPU.

We note that the learning rate hyperparameters for training each method are tuned via a loss computed on observational *validation* data (Eq. (14) with validation observations), which makes these hyperparameter choices subject to random noise in the data. Therefore, this approach may lead to suboptimal parameter choices. However, this approach is what a practitioner would have access to in a real setting. We additionally note that AD-EnKF and AD-Ens3DVar are trained with a fixed ensemble size in an effort to fairly compare the methods. This choice, however, makes AD-Ens3DVar more computationally expensive since an additional C_ϕ matrix needs to be learned, but generally in practice, one may be able to learn from smaller ensemble sizes while maintaining some performance threshold.

Learning ϕ in AD-EnKF (modified). Across all AD-EnKF (modified) experiments, the covariance inflation factor is learned, which is a positive scalar; therefore, we learned a “latent” representation of this scalar that is allowed to take any value on the real line, and the covariance inflation is computed to be a transformation of this quantity that maps it to $[0, 1]$. More formally, we indirectly optimize ϕ by optimizing a latent $\tilde{\phi}$ and applying the transformation $\phi := \text{Sigmoid}(\tilde{\phi})$.

Learning ϕ_1 in AD-Ens3DVar. Similarly, across all AD-Ens3DVar experiments, the covariance mixing parameter is learned, which is another positive value in $[0, 1]$. We similarly learn a “latent” representation of this scalar that can take any value on the real line, and we define a transformation that maps this value to $[0, 1]$. More specifically, we optimize a latent $\tilde{\phi}_1$ such that $\phi_1 = \text{Sigmoid}(\tilde{\phi}_1)$.

Learning θ_2 in AD-Ens3DVar and AD-EnKF. In both AD-Ens3DVar and AD-EnKF, we learn the forecast error covariance Q_{θ_2} parameterized by θ_2 . Across all experiments, we specify that this matrix is diagonal with strictly positive elements along the diagonal. To ensure that the diagonals are strictly positive, we specify that $Q_{\theta_2} = \text{diag}(\text{Softplus}(\theta_2))$ for $\theta_2 \in \mathbb{R}^{d_x}$.

Evaluating the learned covariance inflation factor ϕ in AD-EnKF and the learned covariance mixing parameter ϕ_1 in AD-Ens3DVar. Figure 12 visualizes how close to optimal the learned covariance inflation factors are for AD-EnKF across the three examples, as well as how close to optimal the learned covariance mixing parameters are for AD-Ens3DVar across the three examples. Since we learn from noisy, potentially sparse observations in a joint optimization with both forecast and filtering parameters, the converged values for these parameters are close to but not exactly optimal.

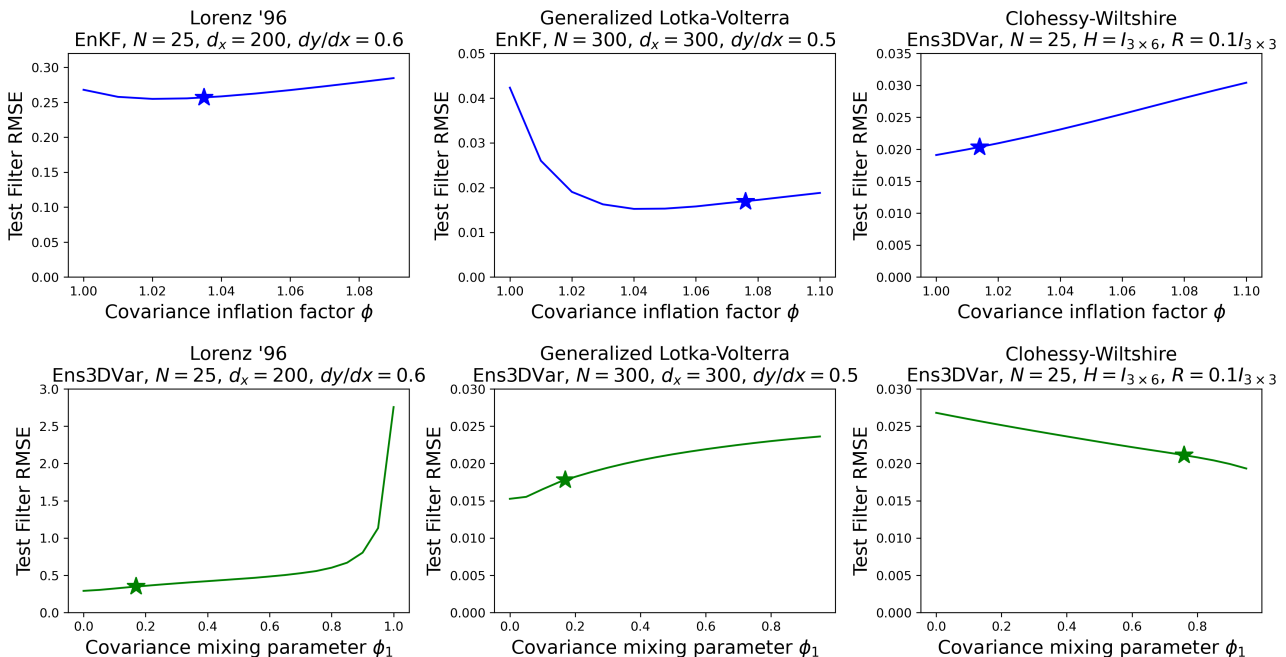


Figure 12: Visualization of the test filter RMSEs across examples and methods. The lines in each plot correspond to the test filter RMSE across parameter choices for either the covariance mixing parameter ϕ_1 in Ens3DVar or the covariance inflation factor ϕ in EnKF. The top row corresponds to filtering results using EnKF, the bottom row corresponds to filtering results using Ens3DVar, and each column corresponds to results from one of our experimental examples. The star in each plot corresponds to the value chosen by the learning algorithm. The EnKF evaluations use the learned forecast parameters $\hat{\theta}$ in the filter, and the Ens3DVar evaluations use both the learned forecast parameters $\hat{\theta}$ and the learned 3DVar background covariance parameters ϕ_2 in the filter.

F.1 Clohessy-Wiltshire

F.1.1 Data generation

We specify that the true parameter that we want to recover is $\theta^* = 0.0013$. The system is observed with a time step $\Delta t = 10$. All experiments are trained with $T = 800$ time points, where 8 independent trajectories of length T were used for training, 4 independent trajectories of length T were used for validation, and 4 independent trajectories of length T were used for testing.

F.1.2 Training details

The subsequence length L for the maximum number of assimilation time points before auto-differentiating is set to $L = 20$ for all experiments. To construct H when $d_y/d_x < 1$, we systematically remove observability, where for example, if $d_y/d_x = 0.66$, we do not observe every third dimension of the state.

For AD-3DVar- C experiments, we initialize $B_{\phi^{(0)}}$ as $0.1I_{d_x}$, for AD-3DVar- K experiments, we initialize $K_{\phi^{(0)}}$ as $H = 0.1I_{d_y, d_x}$, for AD-EnKF experiments, we initialize $\hat{C}_0 := 5I_{d_x \times d_x}$ and the covariance inflation factor $\phi = 0.1$, and for AD-Ens3DVar experiments, we initialize $\tilde{C}_0^{\theta, \phi}$ with $B_{\phi_2} := 0.1I_{d_x \times d_x}$, the covariance mixing parameter $\phi_1 := 0.5$, and $\hat{C}_0 := 5I_{d_x \times d_x}$. For both AD-EnKF and AD-Ens3DVar, we initialize $Q_{\theta_2^{(0)}} = 0.1I_{d_x \times d_x}$. The initial condition x_0 is drawn from the distribution $\mathcal{N}(x_0^*, \tilde{C}_0^{\theta, \phi})$, where $x_0^* = [1.0, 0.5, 1.0, -0.001375, -0.000275, -0.001375]^\top$, which provides a perturbation of the true initial state x_0^* .

We also note that the learnable forecast parameter θ_1 is a strictly positive number. In order to strictly enforce this property, we learned a latent representation of this parameter, denoted as $\hat{\theta}_1$, such that $\theta_1 = \text{Softplus}(\hat{\theta}_1)$. We directly optimize $\hat{\theta}_1$, and feeding this parameter through the Softplus operation ensures that θ_1 is always positive.

F.1.3 Additional filtering visualization

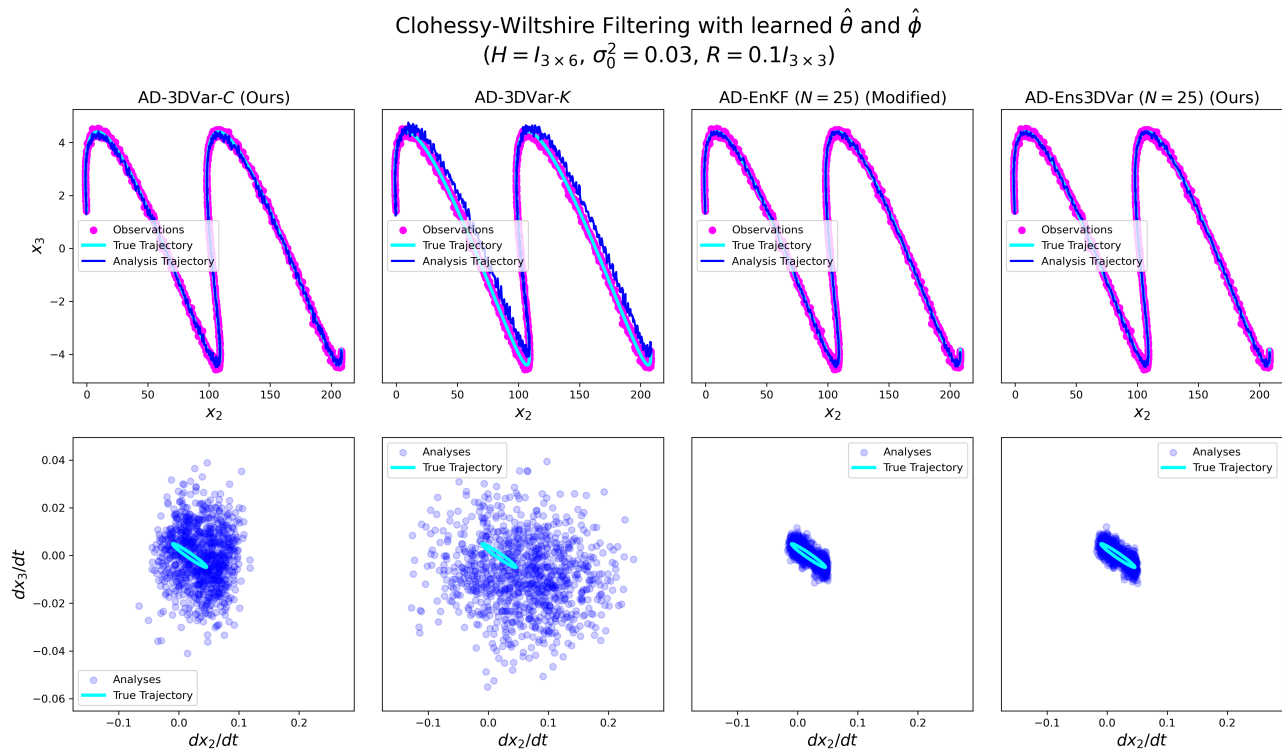


Figure 13: Clohessy-Wiltshire filtering (Section 4.1). Visualization of observations, true trajectories, and estimated positions for y and z , and velocities $\frac{dy}{dt}$ and $\frac{dz}{dt}$ across each of the four filtering methods using the learned forecast parameters $\hat{\theta}$ and learned filtering parameters $\hat{\phi}$, evaluated on test data. In this example, the observation noise is fixed at $R = 0.1I_{d_y \times d_y}$, and the variance of the initialization of $\theta_1^{(0)}$ is fixed at $\sigma_0^2 = 0.03$.

To supplement Figure 2, we additionally plot the observed, filtered, and true y and z positions as well as the filtered and true $\frac{dy}{dt}$ and $\frac{dz}{dt}$ velocities in Figure 13. Similar to the conclusions drawn from Figure 2, AD-EnKF and AD-Ens3DVar accurately recover the positions and velocities with relatively low error. AD-3DVar- C struggles more to estimate the velocity components but can reasonably capture the positions, which suggests that C is reasonably estimated along dimensions where observations are present and struggles otherwise. AD-3DVar- K also struggles to capture the velocity components and additionally shows a bias in its estimates of the position components, which suggests that the estimate of K is suboptimal.

F.1.4 Kalman filter implementation

The Clohessy-Wiltshire equations describe a deterministic *linear* differential equation, where equations (19)-(21) can be rewritten in the notation

$$\frac{d^2x}{dt} = F_{\theta}x, \quad (32)$$

where $\tilde{x} = [x_1, x_2, x_3, \frac{dx_1}{dt}, \frac{dx_2}{dt}, \frac{dx_3}{dt}]$, and $F_\theta \in \mathbb{R}^{6 \times 6}$ is a matrix parameterized by θ . Since these equations are linear, forecasts of this system are provided by the closed-form solution

$$x_{t'+\Delta t'} = e^{F_\theta \Delta t'} x_{t'} \quad (33)$$

for a time step $\Delta t' > 0$, where t' denotes the time of the system (as opposed to the time step t of the filtering process).

The Kalman filter algorithm used to compute the optimal log-likelihood is given in Algorithm 3, where the log-likelihood is given by

$$\mathcal{L}_{\text{KF}}(\theta) := \sum_{t=1}^T \log \mathcal{N}(y_t; H_t \hat{x}_t, H_t P_{t|t}^\theta H_t^\top + R_t), \quad (34)$$

and \hat{x}_t and $P_{t|t}^\theta$ are defined in Algorithm 3. We note that the log-likelihood drops the parameters ϕ since the optimal filtering parameters are specified by the Kalman filter, and therefore do not need to be learned or prespecified.

Algorithm 3 Kalman filter (Kalman, 1960)

Input: Initialization x_0 , observations $y_{1:T}$, observation matrices $H_{1:T}$, observation error matrices $R_{1:T}$, forecast matrix $e^{F_\theta \Delta t'}$ with timestep $\Delta t'$, initialization error covariance matrix P_0

for $t = 1, \dots, T$ **do**

 # Compute the forecast mean and covariance

$$\hat{x}_t = e^{F_\theta \Delta t'} x_{t-1}$$

$$P_{t|t-1}^\theta = (e^{F_\theta \Delta t'}) P_{t-1|t-1}^\theta (e^{F_\theta \Delta t'})^\top$$

 # Compute the Kalman gain

$$K_t = P_{t|t-1}^\theta H_t^\top (H_t P_{t|t-1}^\theta H_t^\top + R_t)^{-1}$$

 # Compute the analysis and analysis covariance

$$x_t = \hat{x}_t + K_t (y_t - H_t \hat{x}_t)$$

$$P_{t|t}^\theta = (I - K_t H_t) P_{t|t-1}^\theta (I - K_t H_t)^\top + K_t R_t K_t^\top$$

end for

Output: Analysis estimates $x_{1:T}$

Figure 14 supplements Figure 3 by visualizing how each component contributes to the overall computed log-likelihood values. Interestingly, the covariance learned from AD-3DVar-C is the closest match to the true $-\frac{1}{2} \log \det S_t$ given by the Kalman filter using the true forecast parameters θ^* , and both AD-EnKF and AD-Ens3DVar provide noisier and more biased estimates of this quantity. However, if we visualize the contribution of the $-\frac{1}{2} \|y_t - H_t \hat{m}_t^\theta\|_{S_t}^2$ term to the overall log-likelihood, we can see that AD-3DVar-C provides much noisier estimates, which ultimately dominates the computed error in the log-likelihood computation shown in Figure 3. Both AD-EnKF and AD-Ens3DVar better estimate this term given by the optimal Kalman filter and show similar noise levels.

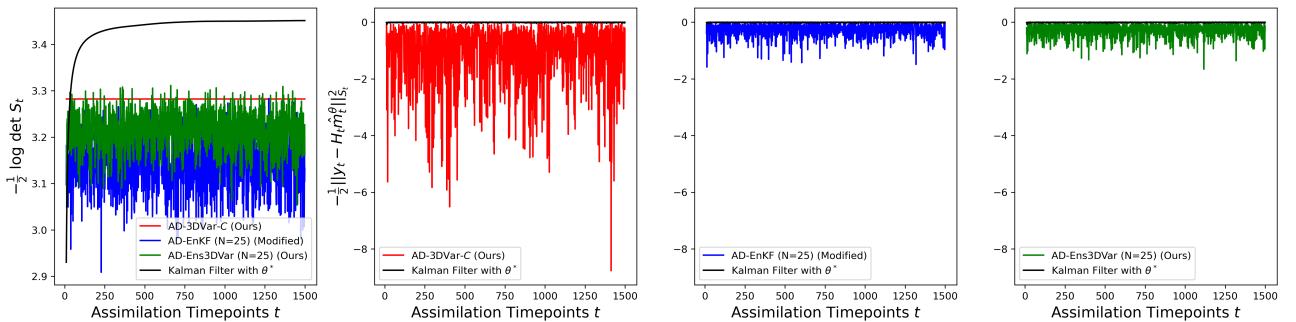


Figure 14: Visualization of each component of the forecast log-likelihood evaluated at observations, given in (14) for filtering with the learned $\hat{\theta}$ and $\hat{\phi}$ from AD-3DVar-C, AD-EnKF, and AD-Ens3DVar compared to the optimal Kalman filter. **(Left)** Component of the log-likelihood that computes $-\frac{1}{2} \log \det S_t$ for each time t . **(Right three)** Residual component of the loss that computes $-\frac{1}{2} \|y_t - H_t \hat{m}_t^\theta\|_{S_t}^2$ for each time t .

F.2 Lorenz-96

F.2.1 Data generation

We implement the Lorenz-96 system with a forcing term $F = 8$, which elicits chaotic behavior of the system. The system is solved with a fourth-order Runge-Kutta (RK4) solver with time step $\Delta t = 0.05$, which is the same time step assumed for observations to arrive. All experiments are trained with $T = 1,200$, where 8 independent trajectories of length T were used for training, 4 independent trajectories of length T were used for validation, and 4 independent trajectories of length T were used for testing.

F.2.2 Training details

The subsequence length L for the maximum number of assimilation time points before auto-differentiating is set to $L = 20$ for all experiments. For AD-3DVar- C experiments, we initialize $C_{\phi^{(0)}}$ as I_{d_x} , for AD-3DVar- K experiments, we initialize $K_{\phi^{(0)}}$ as $H = I_{d_y, d_x}$, for AD-EnKF experiments, we initialize $\hat{C}_0 := 25I_{d_x \times d_x}$ and $\phi = 0.1$, and for AD-Ens3DVar experiments, we initialize $\tilde{C}_0^{\theta, \phi}$ with $C_{\phi_2} := I_{d_x \times d_x}$, $\phi_1 := 0.5$, and $\hat{C}_0 := 25I_{d_x \times d_x}$. For AD-EnKF and AD-Ens3DVar experiments, we utilize the Gaspari-Cohn tapering matrix (Gaspari and Cohn, 1999) with a tapering radius of 5, and initialize $Q_{\theta_2^{(0)}} = 2I_{d_x \times d_x}$. Lastly, the initialization x_0 is randomly drawn from $\mathcal{N}(0, \tilde{C}_0)$, which indicates a lack of knowledge in the initial condition.

F.3 Generalized Lotka-Volterra

F.3.1 Data generation

The generalized Lotka-Volterra equations are solved with a fourth-order Runge-Kutta (RK4) solver with time step $\Delta t = 0.05$, which is the same time step assumed for observations to arrive. For all experiments, for a particular choice of trajectory length T , 8 independent trajectories of length T were used for training, 4 independent trajectories of length T were used for validation, and 4 independent trajectories of length T were used for testing.

To specify the true values A^* , we specified this matrix to have the same block structure shown in Figure 6 where $a_1^* = a_5^* = a_8^* = a_{10}^* = 0.1$, $a_2^* = a_6^* = a_9^* = 0.05$, $a_3^* = a_7^* = 0.01$, and $a_4^* = -0.04$. To generate a true r^* vector for a fixed value of d_x , a d_x length vector is simulated from a standard Gaussian distribution $\mathcal{N}(0, I_{d_x})$, which we denote as \tilde{x}_s^* . Since x_s^* represents the steady-state species abundances, this vector is strictly non-negative. We form x_s^* as $x_s^* = \text{Softplus}(\tilde{x}_s^*)$, where r^* is then constructed as $r^* = -A^*x_s^*$.

F.3.2 Training details

The subsequence length L for the maximum number of assimilation time points before auto-differentiating is set to $L = 20$ for all experiments. For AD-3DVar- C experiments, we initialize $B_{\phi^{(0)}}$ as $0.1I_{d_x}$, for AD-EnKF experiments, we initialize $\hat{C}_0 := I_{d_x \times d_x}$ and $\phi = 0.1$, and for AD-Ens3DVar experiments, we initialize $\tilde{C}_0^{\theta, \phi}$ with $B_{\phi_2} := 0.1I_{d_x \times d_x}$, $\phi_1 := 0.5$, and $\hat{C}_0 := I_{d_x \times d_x}$. For both AD-EnKF and AD-3DVar experiments, we initialize $Q_{\theta_2^{(0)}} = 0.1I_{d_x \times d_x}$. The initialization x_0 is drawn from $\mathcal{N}(\mathbf{1}_{d_x}, \tilde{C}_0^{\theta, \phi})$.

We also note that the solutions of the generalized Lotka-Volterra equations are strictly positive since the equations describe abundances, so we impose some additional transformations at particular steps of the problem to encourage positive analyses. At steps of the assimilation procedure that require drawing random Gaussian samples, such as in the forecast step $\mathcal{M}_\theta(\cdot)$ and the observation perturbation $\mathcal{Y}(\cdot; R)$ in (4), we feed the value plus the simulated noise thorough the absolute value function.